TASK QUARTERLY 16 No 1, 97–133

NANOMECHANICAL PROPERTIES OF METALLIC *FCC* NANORODS FROM MOLECULAR SIMULATIONS WITH THE SUTTON-CHEN FORCE FIELD

MICHAŁ BIAŁOSKÓRSKI[1,2] AND JAROSŁAW RYBICKI[1,2,3]

[1] *Department of Solid State Physics, Faculty of Applied Physics and Mathematics, Gdansk University of Technology, Narutowicza 11/12, 80-233 Gdansk, Poland*

[2] *TASK Computer Centre, Gdansk University of Technology, Narutowicza 11/12, 80-233 Gdansk, Poland*
m.bialoskorski@task.gda.pl

[3] *Institute of Mechatronics, Nanotechnology and Vacuum Techniques, Koszalin University of Technology, Sniadeckich 2, 75-453 Koszalin, Poland*

(Received 2 December 2011; revised manuscript received 24 January 2012)

Abstract: Basic elastic constants (Young's modulus, Poisson's ratio, shear modulus) were determined for several monocrystalline, metallic (Ni, Cu, Pt, Au) nanorods using molecular dynamics with the Sutton-Chen force field. Stress-strain curves were also calculated and discussed.

Keywords: nanorods, nanomechanical properties, elastic constants, plasticity

1. Introduction

The experimental techniques available today do not allow detailed insights into the structure and properties of individual nanostructures. An additional problem in experimental studies is the fact that it is very difficult to obtain a specific nanostructure of a predetermined size and configuration of atoms in a reproducible manner, which hinders an unambiguous interpretation of repeatable measurement results. As a result of the above, computer simulations constitute an extremely

useful research tool. While results obtained with ab initio approaches, at least in principle, reproduce reality most closely, their poor scaling properties mean they quickly become impractical with increasing number of atoms. The need for a computationally-efficient and correct prediction of the properties of various nanostructures is the reason why fast simulations employing empirical force fields are a particularly convenient tool, especially for the calculation of mechanical properties, where the accurate knowledge of the electronic structure is not essential.

The mechanical properties of nanorods are determined from the normal modes of the rod [1] or from the deflection of a rod fixed at one or both sides [2, 3]. Current methods for manufacturing nanorods do not allow obtaining nanorods with preset parameters [1, 2, 4, 5]. These difficulties are the reason why research is predominantly done by means of numerical experiments [6–10]. The abovementioned works deal with specific, single systems.

This paper presents the results of systematic molecular dynamics (MD) simulations of mechanical properties of selected metallic (Cu, Ni, Au, Pt) nanorods. The calculations of elastic properties were performed for small strains and homogeneous stresses. Such states can be achieved only in two cases – during uniaxial stretching of a cylindrical rod along the axis, and under pure shear. The mechanical properties of crystalline systems with regular structure (*sc*, *fcc*, *bcc*) are fully described by three independent material constants, such as, for instance, Young's modulus, shear modulus and Poisson's ratio. The plastic properties were studied across the entire range: from the yield point to the fracture of the sample. Instantaneous values of relevant physical quantities were densely sampled in the course of a molecular dynamics simulation, and the quoted macroscopic mechanical properties were obtained by appropriate temporal and spatial averaging.

The paper is structured as follows. The employed simulation method, including estimates of the uncertainty of the numerical results will be described in Section 2. Results will be described and discussed in Section 3. A brief Section 4 contains conclusions.

2. Simulation method and its accuracy

2.1. General characteristics of simulations

All the numerical experiments were performed at a temperature of 300 K (a Nose-Hoover thermostat [11, 12] was employed), using the Sutton-Chen potential [13]:

$$U = \varepsilon \sum_i \left[\frac{1}{2} \sum_{j \neq i} \left(\frac{a}{r_{ij}} \right)^n - c \sqrt{\sum_{j \neq i} \left(\frac{a}{r_{ij}} \right)^m} \right] \tag{1}$$

developed for densely packed (*fcc*) metals. In (1) c is a dimensionless parameter, ε is a parameter with dimension of energy, a is the lattice constant, and m and n are positive integers with $n > m$. Two methods to determine the parameters of the potential are in use. The first of these consists in adjusting the parameters in

such a manner that the selected properties of the modelled material should match experimentally obtained values. This method is limited by the small number of properties that can be accurately determined from experiment. Moreover, it is difficult to determine the properties under extreme conditions. A more convenient method to use, which moreover yields better results, consists in determining the parameters of the potential by fitting to the properties of the material determined from quantum-mechanical calculations. By employing quantum-based calculations it becomes possible to determine the parameters for a larger number of cases. The parameters used in the present simulations are summarized in Table 1. These are the parameters calculated in part by comparing the characteristics of crystals with the calculations carried out by quantum-mechanical methods [14].

Table 1. Parameters of the SC potential for the species under study

element	ε [eV]	a [Å]	n	m	c
Ni	$7.3767 \cdot 10^{-3}$	3.5157	10	5	58.693
Cu	$5.7921 \cdot 10^{-3}$	3.6030	10	5	84.843
Au	$7.8052 \cdot 10^{-3}$	4.0651	11	8	53.581
Pt	$9.7894 \cdot 10^{-3}$	3.9163	11	7	96.524

The nanorods subjected to numerical experiments were straight and free of defects. In most cases their length was much larger than the diameter. One simulation run comprised the following steps:

- selecting the parameters of the potential of interatomic interactions corresponding to the crystal structure and the element;
- building the initial atomic configuration;
- application of external load;
- sampling (the method and frequency of recording specific observables).

The subsequent steps in the creation of the selected initial atomic structure included the following:

- generating a geometrically ideal (theoretical) crystal structure;
- relaxing the unconstrained system (*i.e.* in the absence of fixing);
- reading the new lattice constants;
- creating an ideal geometric structure with the new lattice constants;
- relaxing the system with the ends immobilized.

Relaxation was conducted until the system energy stabilized at a constant level. The course of an example relaxation of the system is shown in Figure 1. The samples prepared in this fashion were free of any structural defects, and any stress resulting from the changes in the interatomic distances (compared to the bulk crystal) was relaxed.

The loading of the samples was realized by the application of a constant velocity (parallel to the axis of the rod, z) to the sample ends. This corresponds to a constant strain rate, which in turn is equivalent to a constant rate of increase of the force. By loading the sample in such a way, shock load which could otherwise

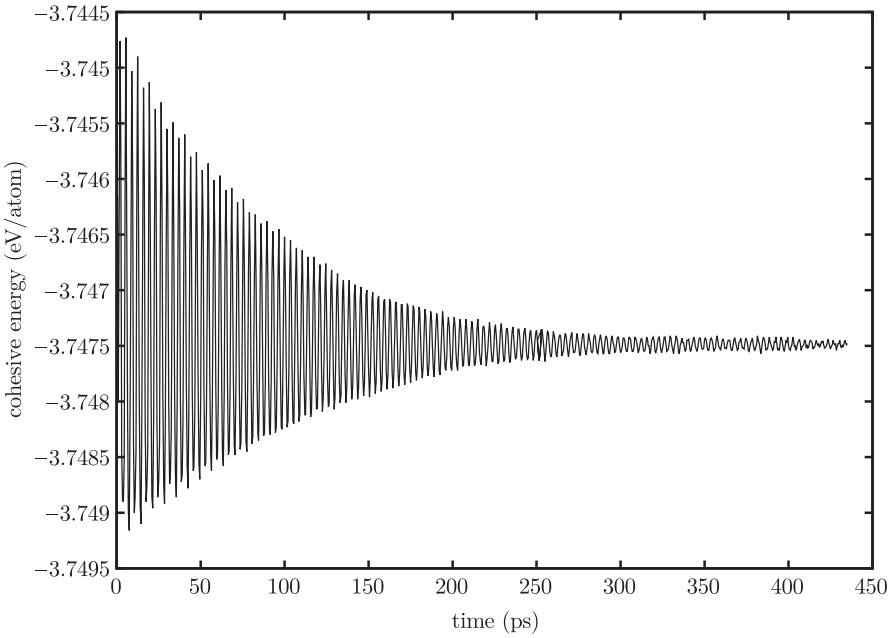

Figure 1. The course of an example nanorod relaxation (rod Au-111-10)

lead to undesirable effects such as vibrations or cracking is eliminated. The details of how the sample was fixed and loaded are discussed in the next chapter.

Saint-Venant's principle states that if a given system of forces acting on a small region of an elastic body (which is in the state of equilibrium) is replaced by another statically equivalent system acting directly on this region, the differences in stress, deformations and displacements at a certain distance from the point of application of the forces, originating from both load cases are arbitrarily small (*i.e.* the impact of the acting forces is averaged).

In the strength of materials it is assumed for rod stretching that it is only at a distance comparable to the rod diameter that the stress field becomes uniform, regardless of how the force is applied to the ends of the rod. In order to remove the possible ways of immobilizing the nanorod ends and the various possible ways to apply the forces and the corresponding nonuniformities of the stress field related thereto from the analysis, rather than fixing the ends in the common sense of the word, we set the relative positions of the last several layers of atoms in the nanorod and applied a constant velocity to the entire nanorod ends. The thickness of the region where the above approach was employed extended over 2–3a.

The external force applied to the end of the rod should be smaller than the sum of the forces binding the end with the rod, *i.e.* the component parallel to the external force being the sum of the interatomic forces responsible for fixing the nanorod. The fact that the magnitude of the thermal motions of atoms exceeds that of the linear motion of the ends makes the vibration amplitude of the whole end larger than the linear step. This is a substantial hurdle in the analysis of data.

All the simulations of nanorods also included the range of plastic strains. The processes occurring in the plastic strain range were carefully analysed by tracking the displacements of atoms with respect to their initial position in the crystal lattice and to the neighbouring atoms. Thus, it was possible to observe the onset and development of slips in stretched and compressed nanorods.

The properties of a nanorod are affected by the cross-sectional shape, size, the arrangement of crystallographic planes with respect to the surface and the cross-section, the details of the surface, porosity, and any deviation from the ideal crystal lattice, and, finally, the element of which the nanorod is built. A large number of factors affecting the variability of mechanical properties renders it necessary to determine the conditions when the variability of the properties is negligible, when all the calculations have a simple form with one variable.

The values obtained by simulation of the plastic range are presented in three ways:

- limit strain (yield point) as a function of the nanorod radius; the adopted parameters were the crystallographic plane and the direction of strain (Figure 2);
- limit stress (yield point) as a function of radius for each element and each crystallographic plane, the adopted parameter was the nanorod radius (Figure 3);
- stress as a function of strain (stretch graphs); the assumed parameter was the crystallographic plane (Figure 4).

2.2. Determination of elastic constants

2.2.1. Determination of Young's modulus

The basic measure characterising the mechanical properties of a material undergoing elastic strain is Young's modulus, Y, indicating the susceptibility of the material to the change of interatomic distances under the applied load.

Young's modulus (and the yield point) were determined from the course of stretching and compression of relaxed samples. The simplest form of the stress-strain relation is Hooke's law for a uniform, uniaxial stress field:

$$\sigma(\varepsilon) = Y\varepsilon \tag{2}$$

where σ – stress, ε – strain. The simulations were carried out until the fracture of the material occurred. A detailed analysis of the results was carried out until dislocations appeared and the corresponding decrease of the internal energy of the sample was observed.

For the range wherein the phenomenon is linear, in order to make a comparison with the macroscopic equivalents of Young's modulus, a straight line must be fitted to the results of the numerical experiment, as shown in Figure 5. Young's modulus for the case of compression (Y_-) and stretching (Y_+) was determined in this way.

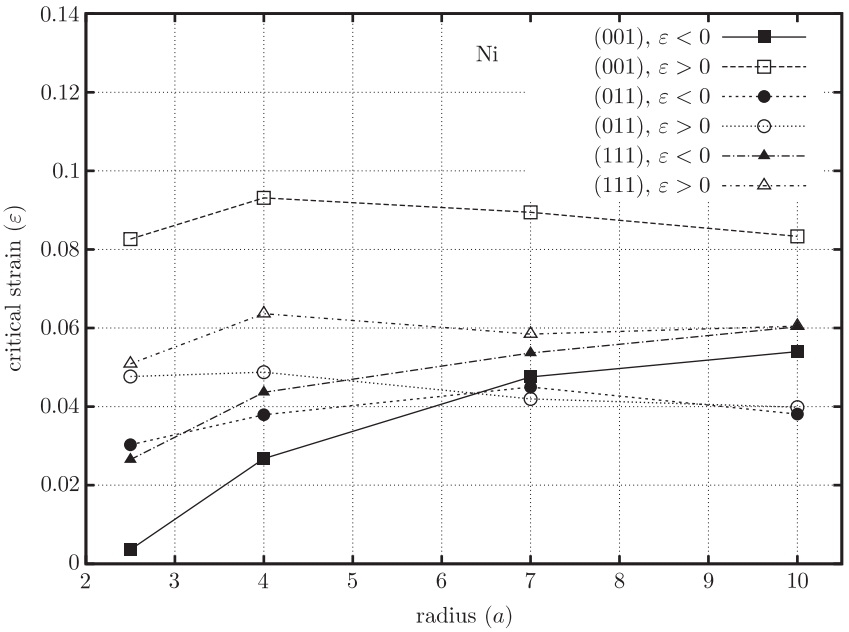

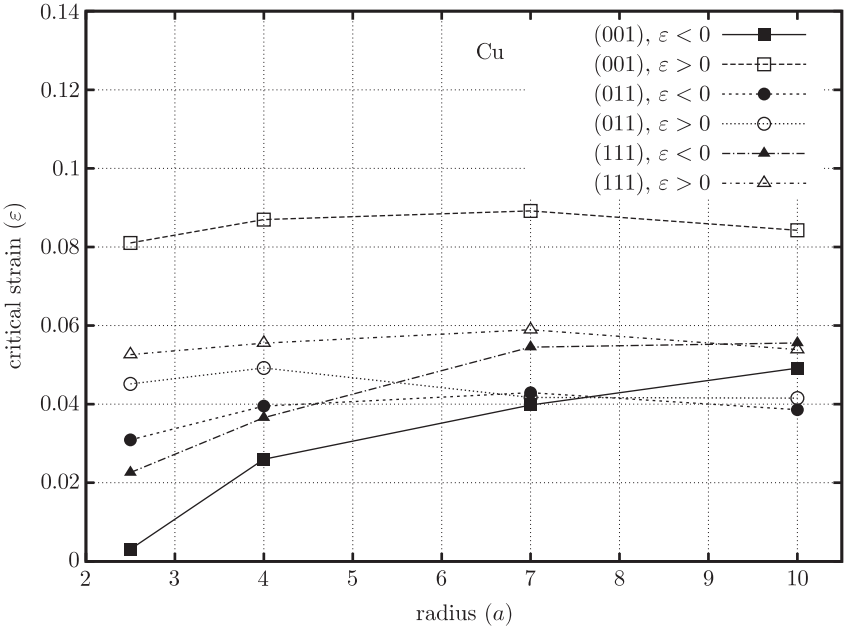

Figure 2. Limit strain (yield point) of the nanorods depending on the radius and the crystallographic orientation of the cross section

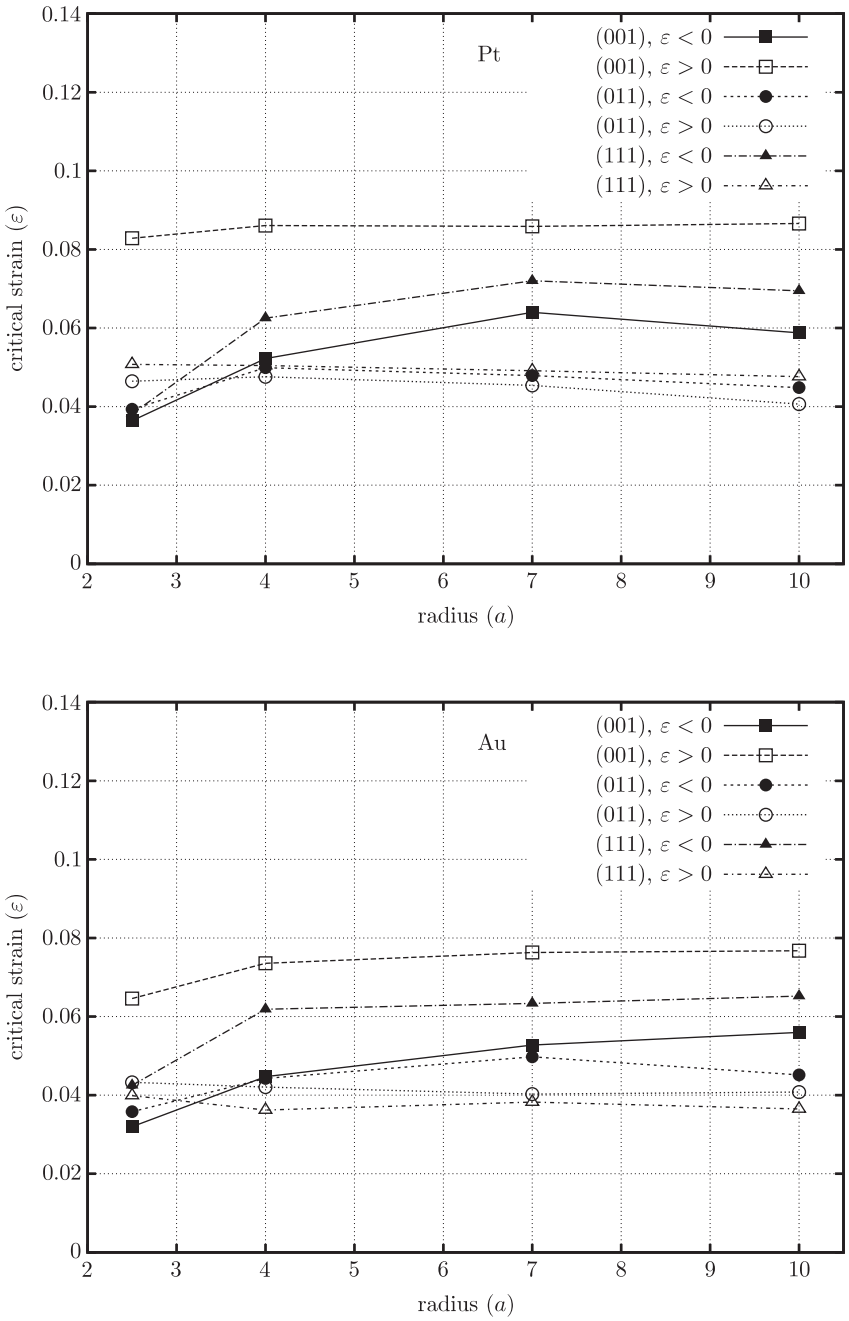

Figure 2 – continued. Limit strain (yield point) of the nanorods depending on the radius and the crystallographic orientation of the cross section

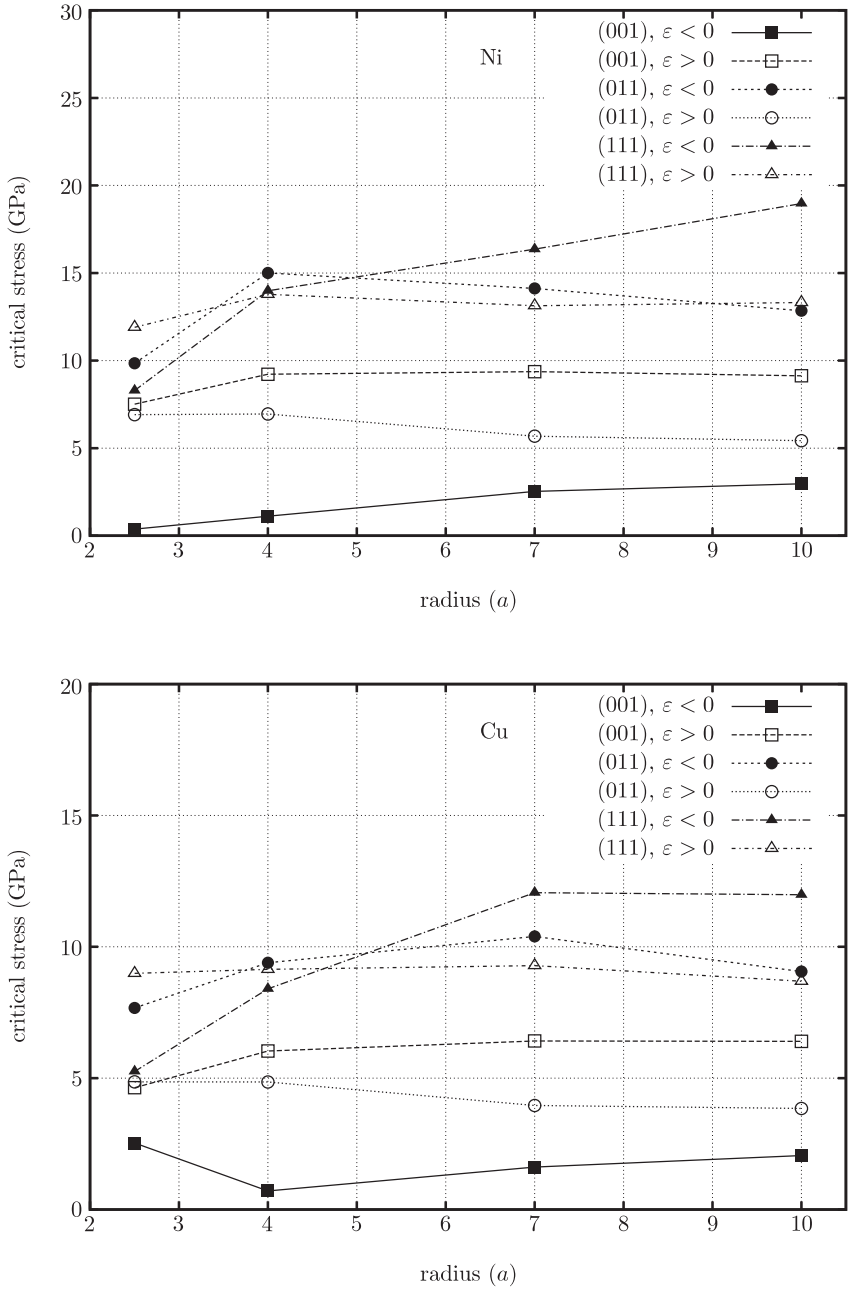

Figure 3. Limit stress (yield point) of the nanorods depending on the radius and the crystallographic orientation of the cross section

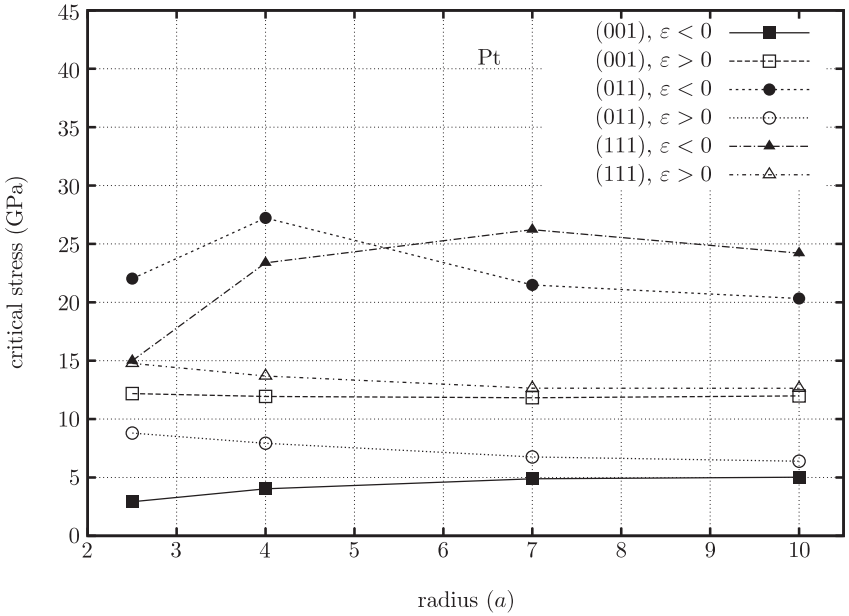

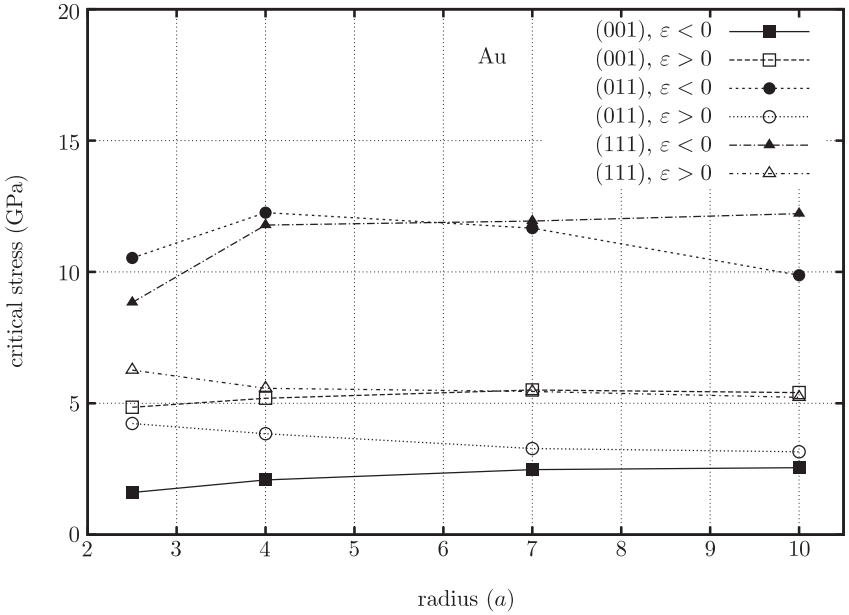

Figure 3 – continued. Limit stress (yield point) of the nanorods depending on the radius and the crystallographic orientation of the cross section

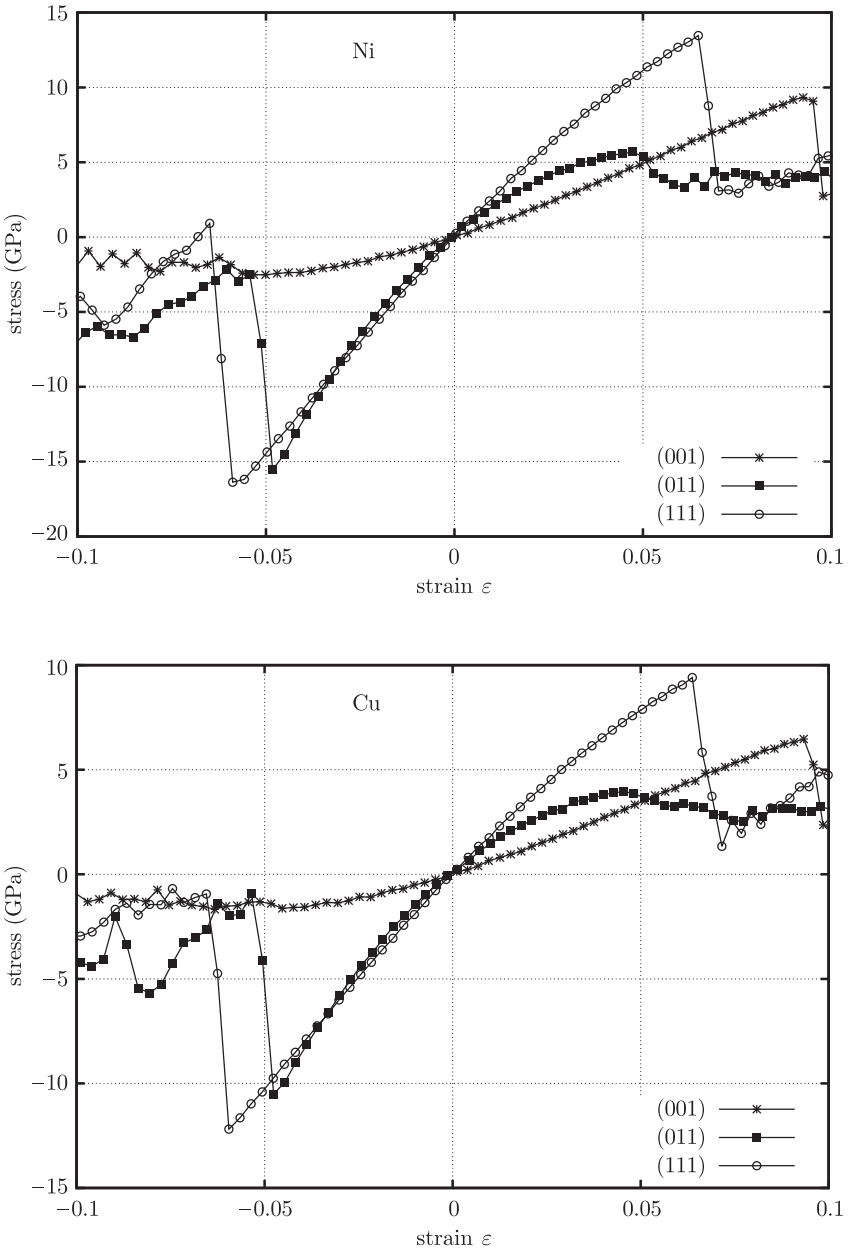

Figure 4. Effect of the crystallographic orientation of the nanorods $D = 14a$ in diameter on the course of deformation

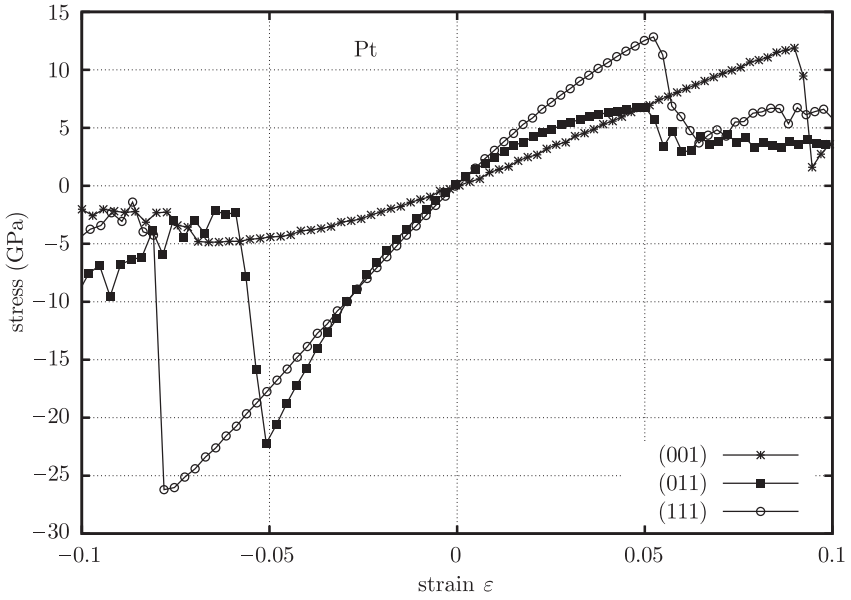

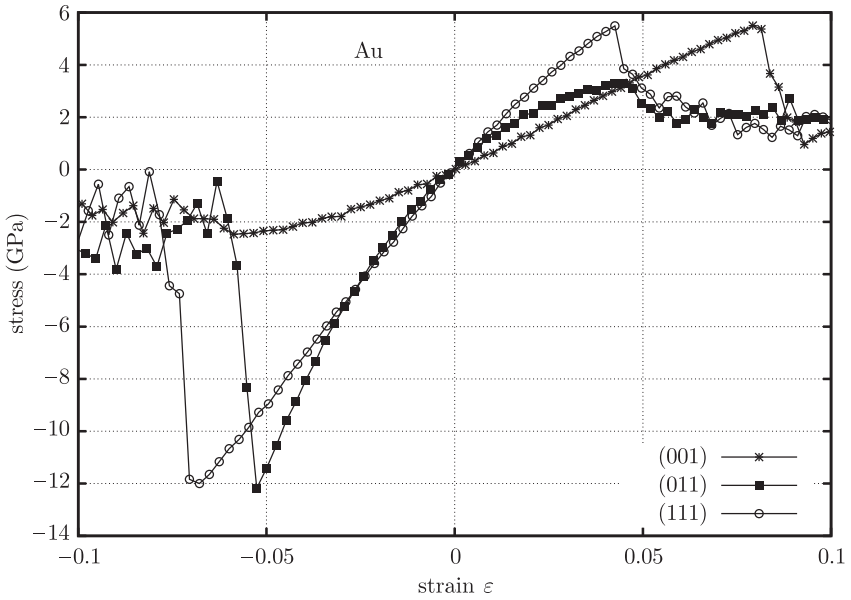

Figure 4 – continued. Effect of the crystallographic orientation of the nanorods $D = 14a$ in diameter on the course of deformation

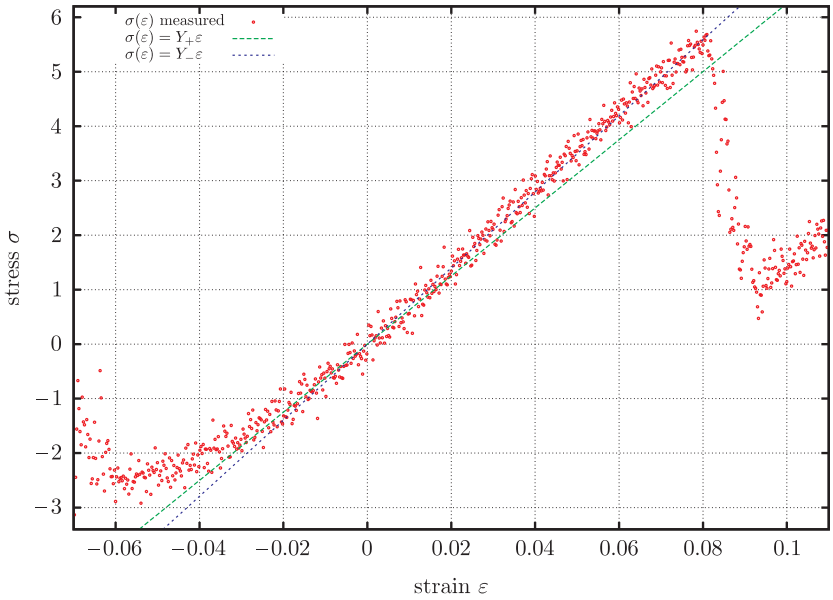

Figure 5. Determination of Young's modulus from the relation $\sigma(\varepsilon)$

2.2.2. Determination of Poisson's ratio

Poisson's ratio characterizes the transverse strain, and for anisotropic systems it depends on the crystallographic directions [15–18]. In *fcc* crystals, where the stretching occurs in the [110] direction, $\varepsilon_x \neq \varepsilon_y$. In this case the determined value is the averaged Poisson's ratio.

In all cases the transverse strain was calculated from the change in the averaged radius of the rod, R, relative to the initial radius R_0:

$$\nu = \varepsilon_r / \varepsilon_z \tag{3}$$

where:

$$\varepsilon_r = \ln\big((R - R_0)/R_0\big) \tag{4}$$

Poisson's ratio was determined directly from the definition, from the dependence of the transverse strain on the longitudinal strain. When the strains are linearly related, Poisson's ratio is equal to the slope. The value of Poisson's ratio determined in this way depends on the linearity range of $\varepsilon_t(\varepsilon_r)$ (*cf.* Figure 6).

2.2.3. Determination of shear modulus

Shear occurs during the torsion of the rod, in the absence of bending and tensile stresses. The shear modulus, G, also called Kirchhoff's modulus, is used to determine the degree to which the material resists such strain. The shear modulus for anisotropic systems is measured for a particular plane along which the shear takes place and for a direction of the applied force or torque.

According to the Cauchy-Born hypothesis, the strain of the entire crystal can be mapped to the edges of unit cells, while the displacement of atoms associated with the face centres is due to the strain of the entire face as a result

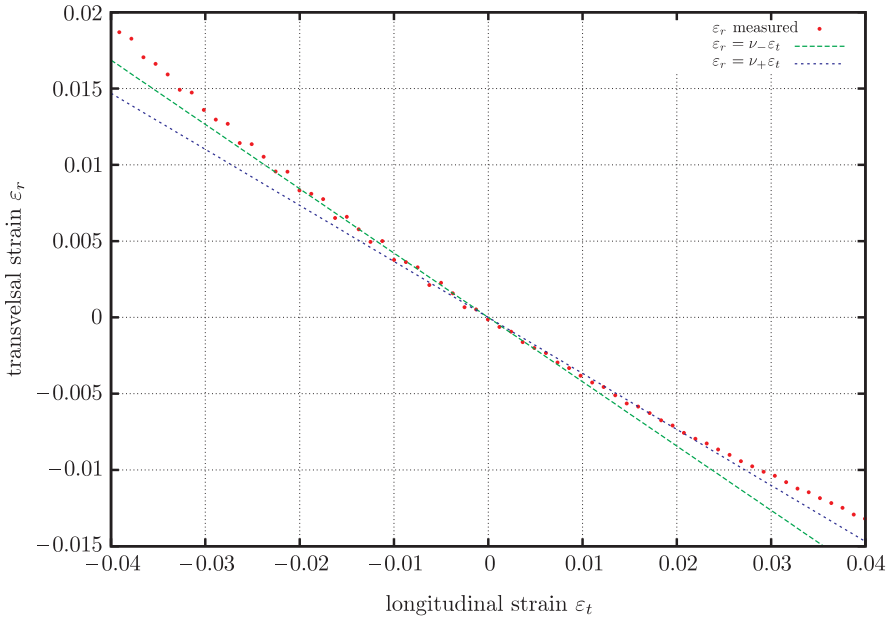

Figure 6. Determination of Poisson's ratio from the relation $\varepsilon_t(\varepsilon_r)$

of the motion of the edges. Under laboratory conditions the shear modulus for massive bodies is determined from the torsion of the rod in a static test in which it is possible to achieve a high accuracy of the measurement.

A different method to determine the shear modulus – from the frequency of torsional vibrations of the rod – was employed during the numerical simulations. After twisting the rod, one of its ends was released and the frequency of the generated torsional vibrations was examined. The shear modulus was calculated using the formula for the fundamental frequency of torsional normal modes of the rod:

$$f = \frac{1}{4L}\sqrt{\frac{G}{\rho}} \tag{5}$$

from which the expression for the shear modulus was obtained:

$$G = 16L^2 f^2 \rho \tag{6}$$

The experiment consisted in twisting the sample by an angle for which an increase in the internal energy was visible, whereupon one of the ends was released. The frequency of torsional vibrations was determined from the period of the oscillations of the internal energy (see Figure 7).

2.2.4. Propagation velocity of mechanical waves

In order to determine the propagation velocity of mechanical waves, the nanorod was stretched by 4%. The release of one of the ends allowed a stepwise decrease the applied force to zero. The moment when the force dropped to zero at

the other, fixed end of the rod was assumed as the moment when this information reached the other end. A plot of the magnitude of the force at the fixed end of the rod is shown in Figure 8.

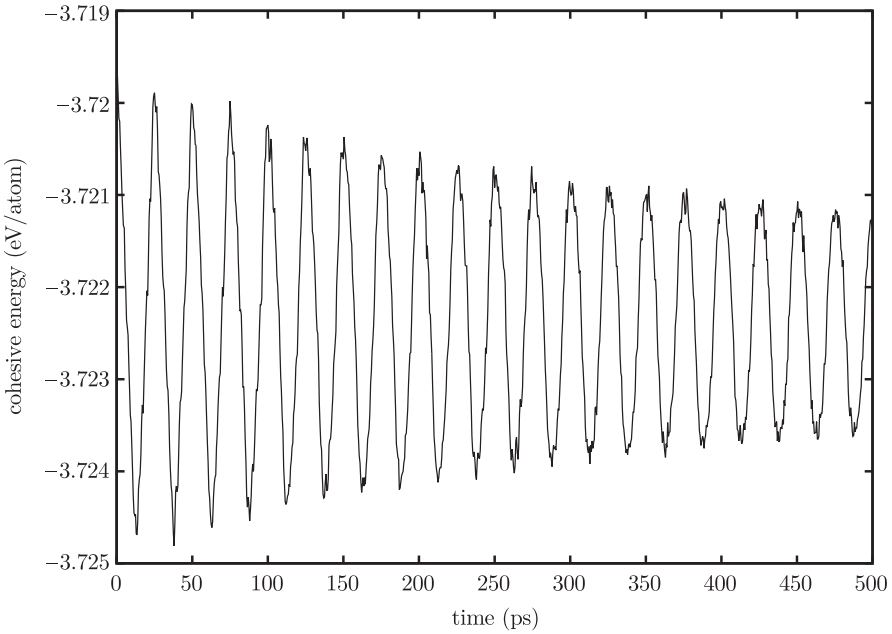

Figure 7. Internal energy of the system during torsional vibration. Example for rod Au-001-7

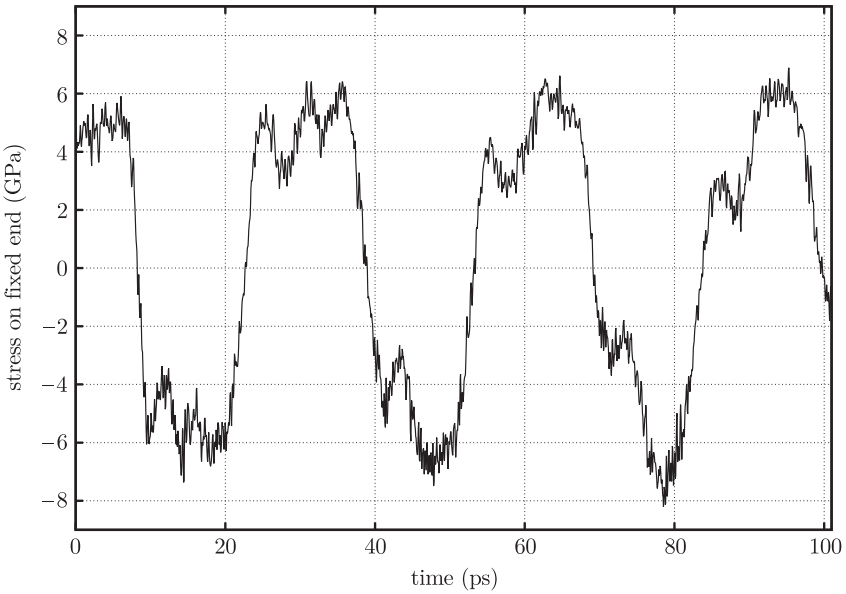

Figure 8. Magnitude of the force acting at the fixed end following the release of the second end, an example for a gold nanorod 208 Å long

The propagation velocity for a mechanical wave travelling in the rod is found from the length of the rod and the propagation time. Table 2 shows the velocities obtained for the rods under study. The propagation velocities obtained in this way were the basis for the validation and possible adjustment of the adopted computational parameters, such as the time step or rate of load increase.

Table 2. Velocity of sound for various nanorods

label	orientation of the cross-section	diameter of the sample [Å]	length of the sample [Å]	sound velocity [m/s]
Au-001-10	(001)	80.2	208.7	1807
Au-011-10	(011)	80.2	208.7	1939
Au-111-4	(111)	31.2	209.3	2490
Au-111-7	(111)	57.6	209.3	2543
Cu-001-10	(001)	71	185.8	2813
Cu-011-10	(011)	71.2	185.8	3205
Cu-111-10	(111)	71	181.4	4258
Cu-111-4	(111)	27.8	186.4	4020
Cu-111-7	(111)	49.2	186.4	4127
Ni-001-10	(001)	69.2	177.0	3342
Ni-011-10	(011)	69.4	176.0	4285
Ni-111-10	(111)	69.2	182.0	5029
Pt-111-4	(111)	30.2	202	3338
Pt-111-10	(111)	77.2	202	3394

2.3. Accuracy of calculations

The determination and quantification of the reliability of computer simulations is known as verification and validation (V & V). Validation is determining the accuracy with which a mathematical model describes the modelled phenomenon. Verification is determining the accuracy with which the computational model represents the mathematical model. Validation ensures the correct equations are solved, while verification ensures these equations are solved correctly [19].

The V & V process can be divided into sections relating to the model and those referring to the data. Validation of the model is the evaluation of the assumptions and methods of representing the problem and testing the model in operation, while verification is the examination of the correctness of implementation. Validation of data is aimed at ensuring that the data used in the model are correct.

In the case of nanostructures it is not possible to conduct V & V to the full extent as the experimental data are subject to considerable uncertainty, in the order of 50%. Comparison against the results of other calculations, which are equally not physically verified, constitutes neither validation nor verification.

The extent of the uncertainty of the results obtained from computer simulations is affected by such factors as:

– the constructed physical model;
– the employed mathematical model;

– the accuracy of the employed numerical methods;
– statistical error;
– repeatability of the simulation.

The employed integration step allowed obtaining stable solutions, and the applied potentials describe the interatomic forces sufficiently well. The statistical error of the obtained results is due to:

– the uncertainty of the geometry measurement;
– the thermal vibrations of the structure.

The thermal vibrations of the structure are a natural phenomenon involving the fluctuations of the measured magnitudes of forces, velocities and positions of atoms. The uncertainty of a calculated value is due to the statistical error committed when averaging the measured parameters of the system or when fitting a functional form to the observed variation of these parameters.

The maximum statistical error, U, observed when determining Young's modulus, resulting from the fitting of a linear relationship to the calculated variation of energy in the function of strain was:

$$U_Y = 10\% \tag{7}$$

and the corresponding value for Poisson's ratio:

$$U_\nu = 6\% \tag{8}$$

In addition to the thermal vibrations, the uncertainty in the measurement of the geometry is also affected by the deviation of the sample shape – a cylinder in the case of the samples under study – from the nominal shape. While the length of the structure can be measured accurately, since it is measured as the distance between the ends that are not subject to any thermal vibration, the diameter of the structure's cross-section is not the same in every direction as is seen in Figure 9. The maximum measurement error of the cross section radius was:

$$\Delta R/R = 2\% \tag{9}$$

Due to the fact that the measured properties also depend on the radius, the effect of this uncertainty should also be taken into account:

$$\Delta Y/Y = 2\Delta R/R + U_Y = 14\% \tag{10}$$

$$\Delta\nu/\nu = \Delta R/|R - R_0| + \Delta R_0/R_0 + U\nu \tag{11}$$

The uncertainty in the measurement of ν is inversely proportional to the difference $R - R_0$, which results in a substantial uncertainty in ν at small strains. For instance, for a strain $\varepsilon_t = 0.02$ $\Delta\nu/\nu|_{\varepsilon_t=0.02} = 20\%$.

The measurement uncertainty of the shear modulus G is related to the accuracy of determining the torsional vibration period and the sample density. The torsional vibration period was determined from 8 periods with an accuracy of up to 1/4 of a period. This gives a relative error in the vibration period of 1/32,

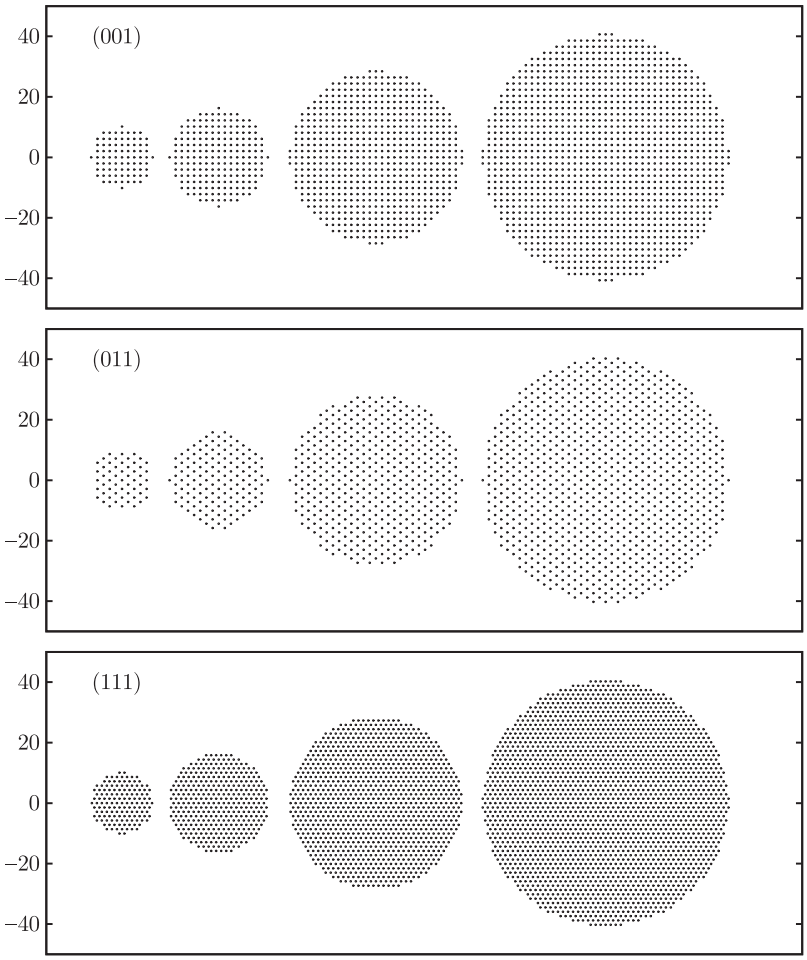

Figure 9. Cross-sections of the nanorods for diameters of $5a$, $8a$, $14a$, $20a$. The cross-sections lie in the (001), (011) and (111) planes, respectively

i.e. $\sim 3\%$, which, following the inclusion of the 4% uncertainty in the density associated with the uncertainty of determining the sample diameter, leads to:

$$\Delta G/G = 7\% \tag{12}$$

The repeatability of the obtained results was verified by comparing the results of several selected simulations with different initial velocities of atoms. The differences in the values of the determined mechanical properties were below the margin of error. The only values exceeding the statistical error of a single measurement were the limit stress σ_{cr} and the limit strain ε_{cr} of the nanostructure. The range of the obtained results was 20%:

$$U(\varepsilon_{cr}) = 20\% \tag{13}$$

which was caused by the dependence of onset of the slip on the thermal fluctuations of atoms.

Table 3. Uncertainties in the determined values describing mechanical properties

parameter	uncertainity
Y	16%
ν	20%
ε_{cr}	20%
G	7%

Table 3 shows the upper estimate of the uncertainty in the determined mechanical properties of the nanostructures.

3. Results and discussion

The numerical experiments were conducted on nanorods with an *fcc* structure that were free of dislocations. The highest possible degree of packing (74%) is the reason why under load it did not reconstruct into other, more densely packed structures.

The tested nanorods were circular in section, made of nickel, copper, platinum and gold. The numerical experiments were performed for crystallographic planes related to the directions of easiest slip, $\langle 011 \rangle$ and $\langle 111 \rangle$, and for the basal directions $\langle 001 \rangle$.

The cross-section of the nanorods under study was chosen to be circular in order to reduce the effect of the planes forming the surface on the results of the experiments. The surface for such a cross-section is formed by many different crystallographic planes parallel to the nanorod axis.

In this way, different nanorods could be compared with no need for separate analysis of the effect of the crystallographic directions on the surface of the side walls [20]. The choice of a circular cross-section was also dictated by the fact that all the nanorods also have circular cross-sections [21]. Finally, the minimum surface energy condition [22] also favours a circular cross section.

The geometric characteristics and the obtained results for nanorods subjected to numerical experiments are summarized in Tables 4 to 7. The diameter of a nanorod resulted from the shape, size and number of lattice constants measured in the plane perpendicular to the axis. The number of lattice constants was selected so that the cross-section would maximally fill a circle circumscribed on a given number of cells. The linear dimensions of the samples in the abovementioned tables were taken as a multiple of the lattice constant in order to facilitate comparison between results obtained for nanorods composed of different elements and for different crystallographic directions. All the samples were 50 lattice constants long, and the diameter of the rods was taken as 3-, 5-, 8-, 14- and 20-multiple of the lattice constant. The experiments were carried out on samples prepared in such a way that the nanorod cross-section coincided with one of the selected crystallographic planes: (001), (011) or (111). All this information is contained in the label, which was constructed as follows: X-(hkl)-R, where: X denotes the element (Au, Ni, Cu, Pt), (hkl) denotes the crystallographic plane perpendicular to the nanorod longitudinal axis, and R is the nanorod radius.

Table 4. The geometric characteristics and the obtained results for Ni nanorods

label	(hkl)	R_0	L_0	ρ_0	Y_s	Y_r	ν_s	ν_r	σ_s	σ_r	G	Y_s/Y_r	ν_s/ν_r	σ_s/σ_r
Ni-001-2.5	001	8.0	167.9	11	0	57	0.70	0.53	0.4	7.5	—	—	1.3	0.0
Ni-001-4	001	13.1	169.9	10	83	80	0.58	0.51	1.1	9.2	—	1.0	1.1	0.1
Ni-001-7	001	24.1	171.9	9	89	124	0.56	0.41	2.5	9.4	125.4	0.7	1.4	0.3
Ni-001-10	001	34.6	172.7	9	93	132	0.57	0.46	3.0	9.1	—	0.7	1.3	0.3
Ni-011-2.5	011	8.5	172.4	11	184	159	0.34	0.32	9.9	6.9	—	1.2	1.1	1.4
Ni-011-4	011	13.0	172.9	10	260	207	0.34	0.33	15.0	7.0	—	1.3	1.0	2.2
Ni-011-7	011	24.0	173.6	9	199	148	0.38	0.39	14.1	5.7	58.2	1.3	1.0	2.5
Ni-011-10	011	34.7	173.9	9	194	136	0.35	0.38	12.9	5.4	—	1.4	0.9	2.4
Ni-111-2.5	111	8.0	173.2	11	249	330	0.37	0.29	8.3	11.9	—	0.8	1.3	0.7
Ni-111-4	111	13.5	173.7	10	285	303	0.36	0.29	14.0	13.8	—	0.9	1.3	1.0
Ni-111-7	111	23.9	174.2	9	261	286	0.35	0.28	16.4	13.1	48.1	0.9	1.3	1.2
Ni-111-10	111	34.6	174.4	9	260	284	0.35	0.27	19.0	13.3	—	0.9	1.3	1.4

Table 5. The geometric characteristics and the obtained results for Cu nanorods

label	(hkl)	R_0	L_0	ρ_0	Y_s	Y_r	ν_s	ν_r	σ_s	σ_r	G	Y_s/Y_r	ν_s/ν_r	σ_s/σ_r
Cu-001-2.5	001	8.2	172.2	11	0	94	0.76	0.54	2.5	4.6	—	—	1.4	0.5
Cu-001-4	001	13.5	174.5	10	64	51	0.58	0.51	0.7	6.1	—	1.3	1.1	0.1
Cu-001-7	001	24.8	176.5	9	67	85	0.57	0.45	1.6	6.4	85.4	0.8	1.3	0.3
Cu-001-10	001	35.5	177.2	9	69	98	0.58	0.44	2.1	6.4	—	0.7	1.3	0.3
Cu-011-2.5	011	8.8	177.0	11	126	98	0.35	0.32	7.7	4.9	—	1.3	1.1	1.6
Cu-011-4	011	13.3	177.5	10	174	115	0.35	0.34	9.4	4.9	—	1.5	1.0	1.9
Cu-011-7	011	24.6	178.2	9	141	95	0.38	0.40	10.4	4.0	39.3	1.5	1.0	2.6
Cu-011-10	011	35.6	178.5	9	139	85	0.36	0.39	9.1	3.9	—	1.6	0.9	2.4
Cu-111-2.5	111	8.2	177.8	11	192	220	0.37	0.26	5.3	9.0	—	0.9	1.4	0.6
Cu-111-4	111	13.9	178.3	10	204	206	0.37	0.29	8.4	9.2	—	1.0	1.3	0.9
Cu-111-7	111	24.6	178.8	9	188	195	0.36	0.28	12.1	9.3	32.4	1.0	1.3	1.3
Cu-111-10	111	35.5	179.0	9	193	196	0.35	0.28	12.0	8.7	—	1.0	1.3	1.4

tq1161-g/115 3I2013 BOP s.c., http://www.bop.com.pl

Table 6. The geometric characteristics and the obtained results for Pt nanorods

label	(hkl)	R_0	L_0	ρ_0	Y_s	Y_r	ν_s	ν_r	σ_s	σ_r	G	Y_s/Y_r	ν_s/ν_r	σ_s/σ_r
Pt-001-2.5	001	8.8	191.0	28	117	142	0.53	0.42	2.9	12.2	—	0.8	1.3	0.2
Pt-001-4	001	14.5	192.5	25	123	154	0.54	0.43	4.0	12.0	—	0.8	1.2	0.3
Pt-001-7	001	26.8	193.5	23	134	154	0.53	0.44	4.9	11.9	116.4	0.9	1.2	0.4
Pt-001-10	001	38.5	193.7	22	133	157	0.55	0.46	5.0	12.0	—	0.8	1.2	0.4
Pt-011-2.5	011	9.5	192.5	26	384	246	0.38	0.36	22.1	8.8	—	1.6	1.1	2.5
Pt-011-4	011	14.4	193.2	25	336	225	0.38	0.38	27.3	7.9	—	1.5	1.0	3.4
Pt-011-7	011	26.8	194.0	22	285	182	0.42	0.43	21.5	6.8	57.1	1.6	1.0	3.2
Pt-011-10	011	38.7	194.0	22	276	176	0.39	0.40	20.3	6.4	—	1.6	1.0	3.2
Pt-111-2.5	111	8.9	193.6	27	378	365	0.41	0.31	15.0	14.8	—	1.0	1.3	1.0
Pt-111-4	111	15.1	194.3	24	349	323	0.40	0.30	23.4	13.7	—	1.1	1.4	1.7
Pt-111-7	111	26.7	194.6	23	336	308	0.40	0.32	26.2	12.6	64.4	1.1	1.3	2.1
Pt-111-10	111	38.7	194.6	22	330	304	0.40	0.32	24.2	12.6	—	1.1	1.3	1.9

Table 7. The geometric characteristics and the obtained results for Au nanorods

label	(hkl)	R_0	L_0	ρ_0	Y_s	Y_r	ν_s	ν_r	σ_s	σ_r	G	Y_s/Y_r	ν_s/ν_r	σ_s/σ_r
Au-001-2.5	001	9.1	199.3	25	83	98	0.55	0.40	1.6	4.9	51.8	0.9	1.4	0.3
Au-001-4	001	15.1	200.6	22	76	94	0.54	0.43	2.1	5.2	54.2	0.8	1.2	0.4
Au-001-7	001	27.9	201.3	20	75	89	0.56	0.48	2.5	5.5	53.5	0.8	1.2	0.4
Au-001-10	001	40.1	201.6	20	78	91	0.55	0.48	2.5	5.4	53.6	0.9	1.1	0.5
Au-011-2.5	011	9.2	199.3	24	214	134	0.47	0.43	10.6	4.2	25.4	1.6	1.1	2.5
Au-011-4	011	15.0	200.8	22	174	103	0.42	0.40	12.3	3.8	32.5	1.7	1.0	3.2
Au-011-7	011	27.9	201.3	20	136	86	0.45	0.45	11.7	3.3	29.6	1.6	1.0	3.6
Au-011-10	011	40.1	201.8	20	137	84	0.42	0.44	9.9	3.2	30.1	1.6	0.9	3.1
Au-111-2.5	111	9.2	201.2	24	198	194	0.45	0.34	8.8	6.3	27.6	1.0	1.3	1.4
Au-111-4	111	15.6	202.0	22	188	171	0.44	0.35	11.8	5.6	27.8	1.1	1.2	2.1
Au-111-7	111	27.8	202.2	20	180	159	0.44	0.35	11.9	5.5	27.5	1.1	1.2	2.2
Au-111-10	111	40.0	202.5	20	183	156	0.43	0.35	12.2	5.2	27.9	1.2	1.2	2.3

tq1161-g/116 3I2013 BOP s.c., http://www.bop.com.pl

3.1. Young's modulus

Young's modulus was studied for nanorods $3a$, $5a$, $8a$, $14a$ and $20a$ in diameter. Figure 10 shows the results obtained using the `nanoMD` program.

The values of Young's modulus for compression and stretching as a function of the radius of the sample for each of the elements under study and for each of the analysed crystallographic planes are shown in Figure 10.

The calculations were performed according to the formula:

$$Y = \frac{1}{V_0} \frac{\partial^2 E}{\partial \varepsilon^2} \tag{14}$$

whereby a parabola was fitted to the measured cohesive energy, $E_p(\varepsilon)$, in the range of $-0.03 < \varepsilon < 0.03$.

The dependence of Young's modulus on the sample diameter is noticeable for samples smaller than $10a$ in diameter. This is due to the surface tension effect.

Further discussion of the results will concern rods $14a$ in diameter. Starting from this diameter there is no significant effect of the surface tension on the properties of the tested material. Samples $20a$ in diameter will be excluded from further analysis because of the possible effect of the fastenings on the mechanical properties, as the D/L ratio was as high as 0.4, irrespective of the fact that such effect was not observed. The obtained values, denoted by Y, are shown in Figure 11.

Irrespective of the building material, and the direction of the load, Young's modulus had the greatest value for the [111] direction and the smallest value for the [001] direction:

$$Y^{(001)} < Y^{(011)} < Y^{(111)} \tag{15}$$

A deviation from this behaviour was observed in the case of gold nanorod stretching where $Y^{(011)}$ was smaller than $Y^{(001)}$. Nonetheless, due to the accuracy of determining this value being 6%, this is exception is within the margin of error.

The following relations were observed for all nanorods during compression:

$$Y_-^{(001)} \approx 0.5 Y_-^{(011)} \approx 0.4 Y_-^{(111)} \tag{16}$$

while the relations during stretching were:

$$Y_+^{(001)} \approx Y_+^{(011)} \approx 0.5 Y_+^{(111)} \tag{17}$$

This demonstrates the variability of loading in the [011] direction depending on whether stretching or compression was performed. Furthermore, by analysing the ratio of Young's modulus for compression to that of stretching in the same direction:

$$\begin{aligned} Y_-^{(001)}/Y_+^{(001)} &\approx 0.8 \\ Y_-^{(011)}/Y_+^{(011)} &\approx 1.5 \\ Y_-^{(111)}/Y_+^{(111)} &\approx 1.0 \end{aligned} \tag{18}$$

we observe a symmetry of Young's modulus for the [111] direction and the largest disproportion for the [011] direction. This is related to the number of

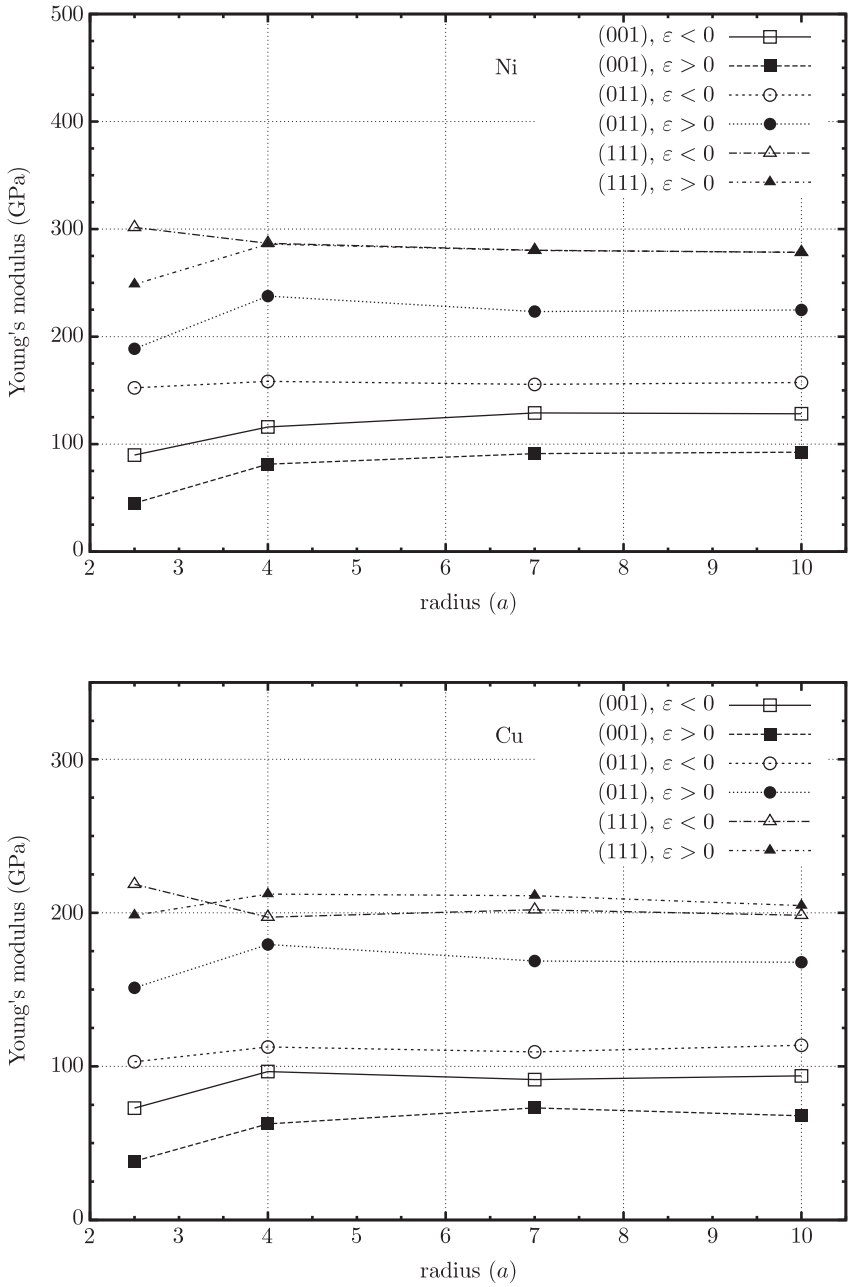

Figure 10. Dependence of Young's modulus on the radius and on the crystallographic orientation of nanorods

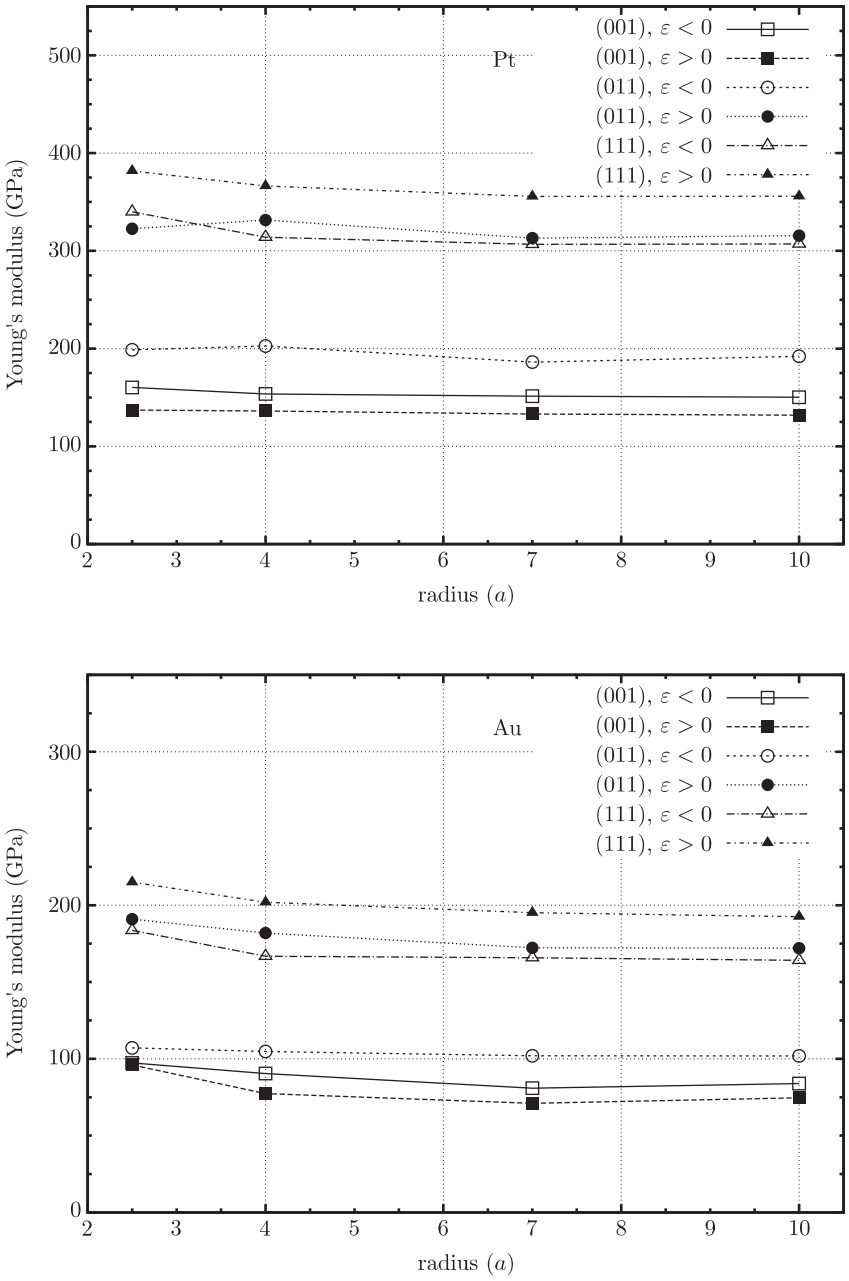

Figure 10 – continued. Dependence of Young's modulus on the radius and on the crystallographic orientation of nanorods

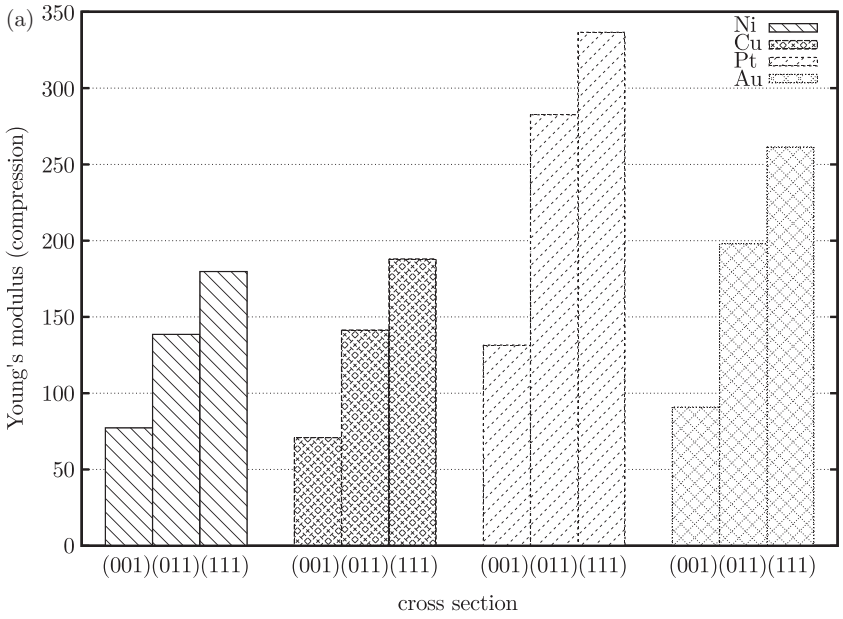

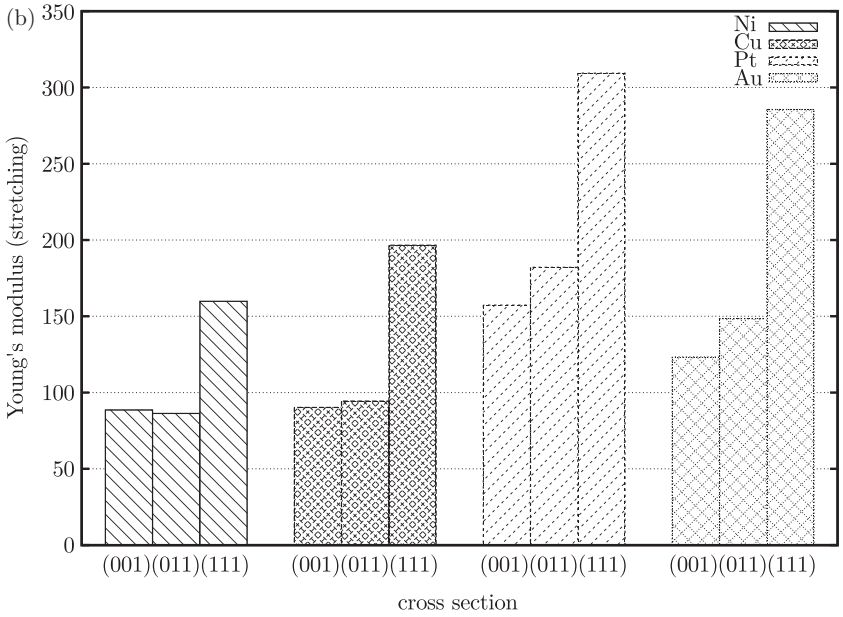

Figure 11. Values of Young's modulus for rods with a diameter $D = 14a$: (a) during compression, (b) during stretching

nearest neighbours in the plane perpendicular to the direction of loading, as the mechanical properties are affected by the local arrangement of atoms, that is, inter alia, the distance to the nearest neighbours.

If the strain of the sample does not result in changes in all distances to the nearest neighbours, and the varying distances change in an identical way, then the sample will be characterised by a symmetrical load curve $\sigma(\varepsilon)$, and the mechanical properties of the sample will be independent of whether the load corresponded to compression or stretching. The [111] direction behaves in this way, while the (011) plane has only two nearest neighbours, and the distances to other neighbours change unevenly during straining. The load curves $\sigma(\varepsilon)$ are shown in Figure 4.

Due to the variability of the slope of the curves $\sigma = f(\varepsilon)$, which can be seen in Figures 4, Young's modulus is a material constant:

- for stretching in the [001] direction;
- for compression in the [011] direction;

while for

- compression in the [001] direction;
- compression and stretching in the [011] direction;
- stretching in the [111] direction

it is not possible to speak about Young's modulus as a material constant, since $Y = Y(\varepsilon)$, $d\sigma/d\varepsilon \neq \text{const}$.

Table 8 summarizes the values of Young's modulus obtained in the numerical simulations carried out on rods $14a$ in diameter for each of the investigated directions and the values calculated according to the formulas:

- for the directions $\langle 001 \rangle$:

$$Y^{(001)} = \frac{1}{s_{11}} \tag{19}$$

- for the directions $\langle 011 \rangle$:

$$Y^{(011)} = \frac{4}{2s_{11} + 2s_{12} + s_{44}} \tag{20}$$

- for the directions $\langle 111 \rangle$:

$$Y^{(111)} = \frac{3}{s_{11} + 2s_{12} + s_{44}} \tag{21}$$

for the elastic constants contained in Table 9.

For each of the elements it is possible to determine the parameters of the polynomial functions describing the relation $\sigma(\varepsilon)$. In the strain range of $-0.01 < \varepsilon < 0.01$ a first-order polynomial describes the $\sigma(\varepsilon)$ curve with an error below 10%, similarly for a second-order polynomial in the range of $0.08\varepsilon_{cr-} < \varepsilon < 0.08\varepsilon_{cr+}$ and for a cubic in the entire range of elastic strain $\varepsilon_{cr-} < \varepsilon < \varepsilon_{cr+}$.

3.2. Poisson's ratio

We will use the following notation: ε_t – the strain along the nanorod (longitudinal strain) parallel to the applied load, ε_r – the transverse (radial)

strain, perpendicular to the direction of the applied load. The values of Poisson's ratio, ν_t, ν_r, ν_- and ν_+ referring to compression and stretching of the sample, respectively, were determined in a similar way.

Table 10 shows Poisson's ratio obtained from calculations using the `nanoMD` program for rods $14a$ in diameter ("simulation result" column) compared with the calculations performed using the elastic constants from Table 9.

Poisson's ratio was determined from the changes in the nanorod radius for strains of $-0.02 < \varepsilon < 0$ for compression and $0 < \varepsilon < 0.02$ for stretching according to the method described in Section 2.2.2.

For the force acting along the [001] and [111] directions Poisson's ratios were constant, regardless of the strain directions which were perpendicular to the direction of force. However, for straining in the [011] direction, the biggest change in diameter occurred only in the [001] crystallographic direction and there was no visible change in the rod diameter $\nu_r^{(0\overline{1}1)} = 1$, $\nu_r^{(001)} = 0$ for the $[0\overline{1}1]$ direction. This is a consequence of the asymmetry of Young's modulus for these directions (16) – the [001] direction undergoes greater strain than the $[0\overline{1}1]$ direction at the same radial stress.

Due to the fact that the materials are usually defined by a single parameter, the value $\nu^{(011)}$ was calculated as an average of the full range of the angle of rotation around the rod axis.

In all cases Poisson's ratio was the highest for the [001] direction and the lowest for the [111] direction:

$$\nu^{(001)} > \nu^{(011)} > \nu^{(111)} \tag{22}$$

which is shown in Figure 12. These inequalities are reversed when compared to analogous inequalities for the value of Young's modulus (15). This means that the strain in the direction with lower Young's modulus results in a greater change in the sample's diameter than the strain in the direction characterised by higher Young's modulus.

In contradistinction to the relation for Young's modulus (16) and (17), the relation for Poisson's ratios between the directions depends on the element of which the sample is composed.

The following is observed for nickel and copper:

$$\begin{aligned} \nu_-^{(001)} &\approx 1.4\nu_-^{(011)} \approx 1.6\nu_-^{(111)} \\ \nu_+^{(001)} &\approx 1.2\nu_+^{(011)} \approx 1.6\nu_+^{(111)} \end{aligned} \tag{23}$$

while for platinum and gold:

$$\begin{aligned} \nu_-^{(001)} &\approx 1.2\nu_-^{(011)} \approx 1.3 - \nu_-^{(111)} \\ \nu_+^{(001)} &\approx 1.2\nu_+^{(011)} \approx 1.4\nu_+^{(111)} \end{aligned} \tag{24}$$

Furthermore, for the strain directions [011] and [111]:

$$\nu_{\mathrm{Ni}} < \nu_{\mathrm{Cu}} < \nu_{\mathrm{Pt}} < \nu_{\mathrm{Au}} \tag{25}$$

Table 8. Values of Young's modulus (GPa) for the investigated nanorods

element	$Y^{(001)}$			$Y^{(011)}$			$Y^{(111)}$			polycristals, tables
	tables	simulation result		tables	simulation result		tables	simulation result		
		stretching	compression		stretching	compression		stretching	compression	Y_b
Ni	129	132	93	212	136	194	304	284	260	200
Cu	66	98	69	122	139	179	191	196	193	130
Pt	136	157	133	175	176	276	210	304	330	168
Au	43	91	78	76	84	137	116	156	183	78

Table 9. Selected values and ratios of elastic constants for the investigated elements according to the tabular data for bulk systems. The table shows the following: the atomic number (la), atomic mass (ma), smallest interatomic distance in *fcc* lattices Å ($l_{\min}$), density ρ in kg/dm^3, melting point (T_t) and boiling point (T_b) in K, sound velocity (ν_{dz}) in m/s and elastic susceptibility s_{ij} in TPa^{-1} (acc. to [23]). The relations given in the publications [15–18] will be used to calculate the material constants Y, G and ν for other crystallographic planes

element	la	ma	l_{min}	ϱ	T_t	T_b	ν_{dz}	s_{11}	s_{12}	s_{44}
Ni	28	59	2.492	10.94	1728	3186	4970	7.75	−2.98	8.05
Cu	29	63.5	2.556	11.81	1358	2840	3570	15.25	−6.39	13.23
Pt	78	195.1	2.775	15.1	2041	4098	2680	7.34	−3.08	13.07
Au	79	197	2.884	16.96	1337	3129	1740	23.3	−10.65	23.8

Table 10. Values of Poisson's ratio for the investigated nanorods

element	$\nu^{(001)}$			$\nu^{(011)}$			$\nu^{(111)}$			polycristals, tables
	tables	simulation result		tables	simulation result		tables	simulation result		
		stretching	compression		stretching	compression		stretching	compression	ν_b
Ni	0.38	0.46	0.57	0.30	0.38	0.35	0.23	0.27	0.35	0.31
Cu	0.42	0.44	0.58	0.34	0.39	0.36	0.26	0.28	0.35	0.35
Pt	0.42	0.46	0.55	0.39	0.40	0.39	0.38	0.32	0.40	0.38
Au	0.45	0.48	0.55	0.42	0.44	0.42	0.38	0.35	0.43	0.44

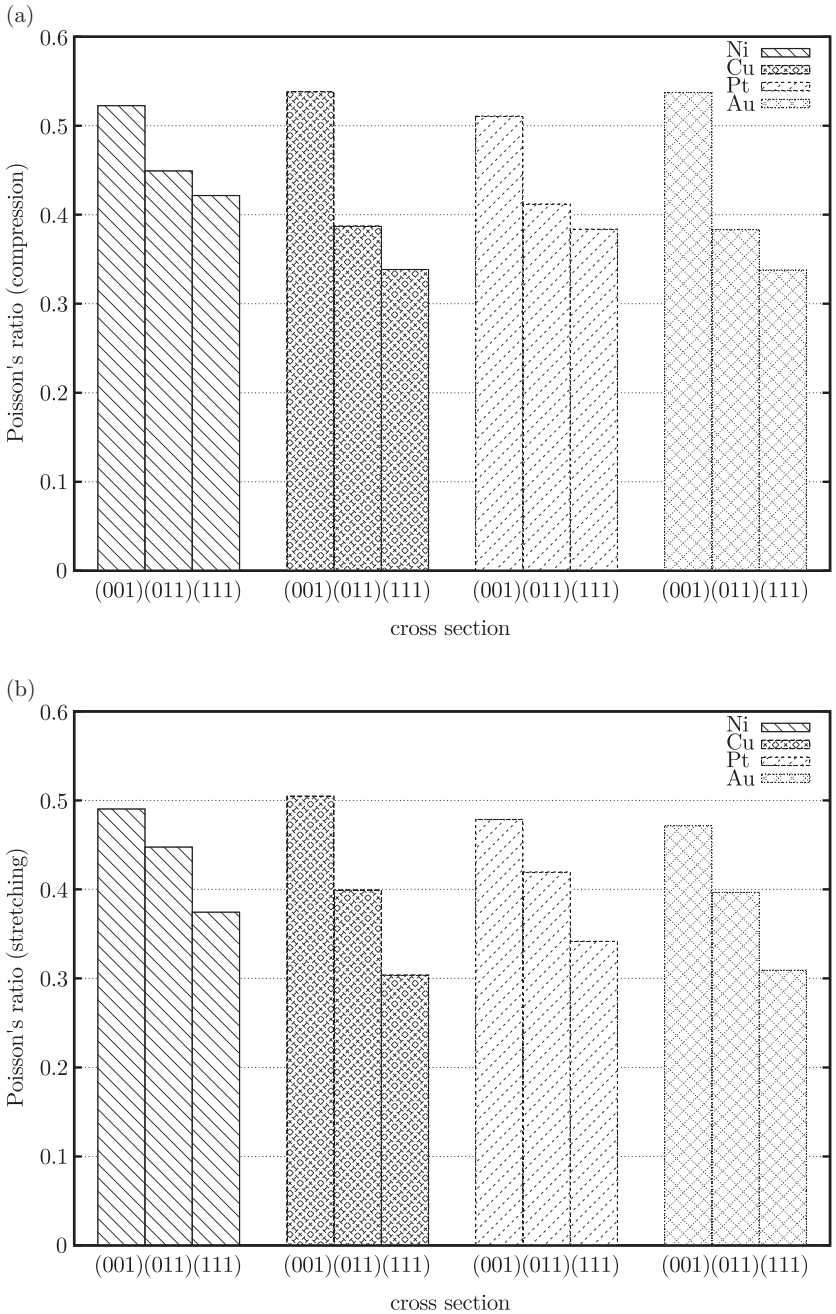

Figure 12. Values of Poisson's ratio for rods $D = 14a$ in diameter: (a) during compression, (b) during stretching

which shows the effect of the density and the material on Poisson's ratio. Atoms of a less dense medium have more space to move, and therefore strain in the given direction results in less strain in the perpendicular plane than in a denser medium.

The lack of clear stabilization of Poisson's ratio with the increasing sample diameter can be seen in Figure 13 showing the value of ν for compression and stretching as a function of the rod radius expressed in lattice constants a. This is due to the error of $\pm 10\%$ in the determination of the value.

All the test samples subjected to a compressive load acting in the [001] direction showed values of ν greater than 0.5. This demonstrates the increasing volume of the nanorod during compression and cannot be justified on the grounds of classical mechanics. This is not an effect of the larger rod diameter relative to length as it persisted for all the tested diameters. It is evident from Figure 14 showing the dependence of the change in the sample radius (transverse strain ε_r) on longitudinal strain ε_t, that the curve slope increases with the increasing strain, which means that Poisson's ratio increases with increasing strain.

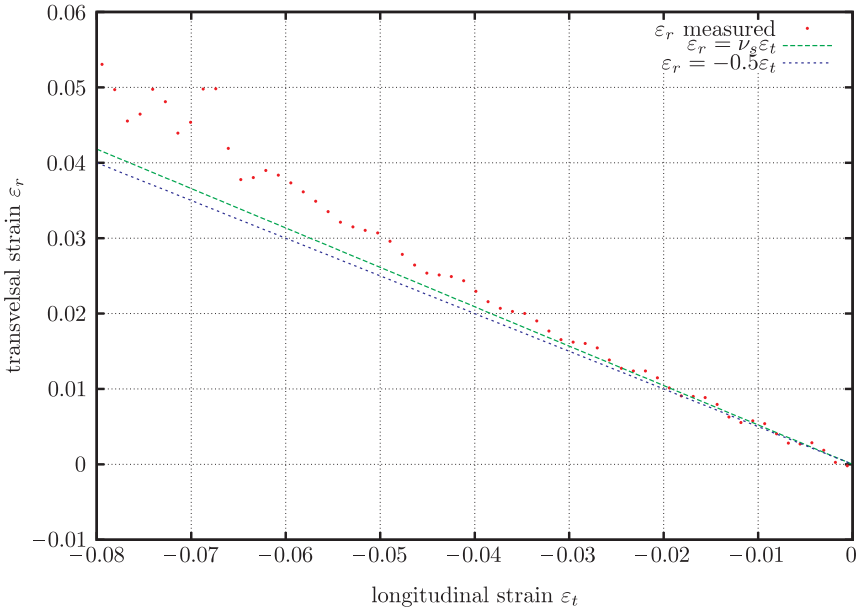

Figure 14. Dependence of the transverse strain ε_r on the longitudinal strain ε_t for the compression of gold nanorod in the [001] direction

3.3. Shear modulus

The shear modulus was determined from the frequency of torsional vibration of the rod according to the Formula (5). The results obtained in this way determine the average value of the modulus from all the directions perpendicular to the axis of the rod. For that reason, in order to determine this value it is sufficient to indicate the adopted crystallographic orientation of the nanorod cross-section.

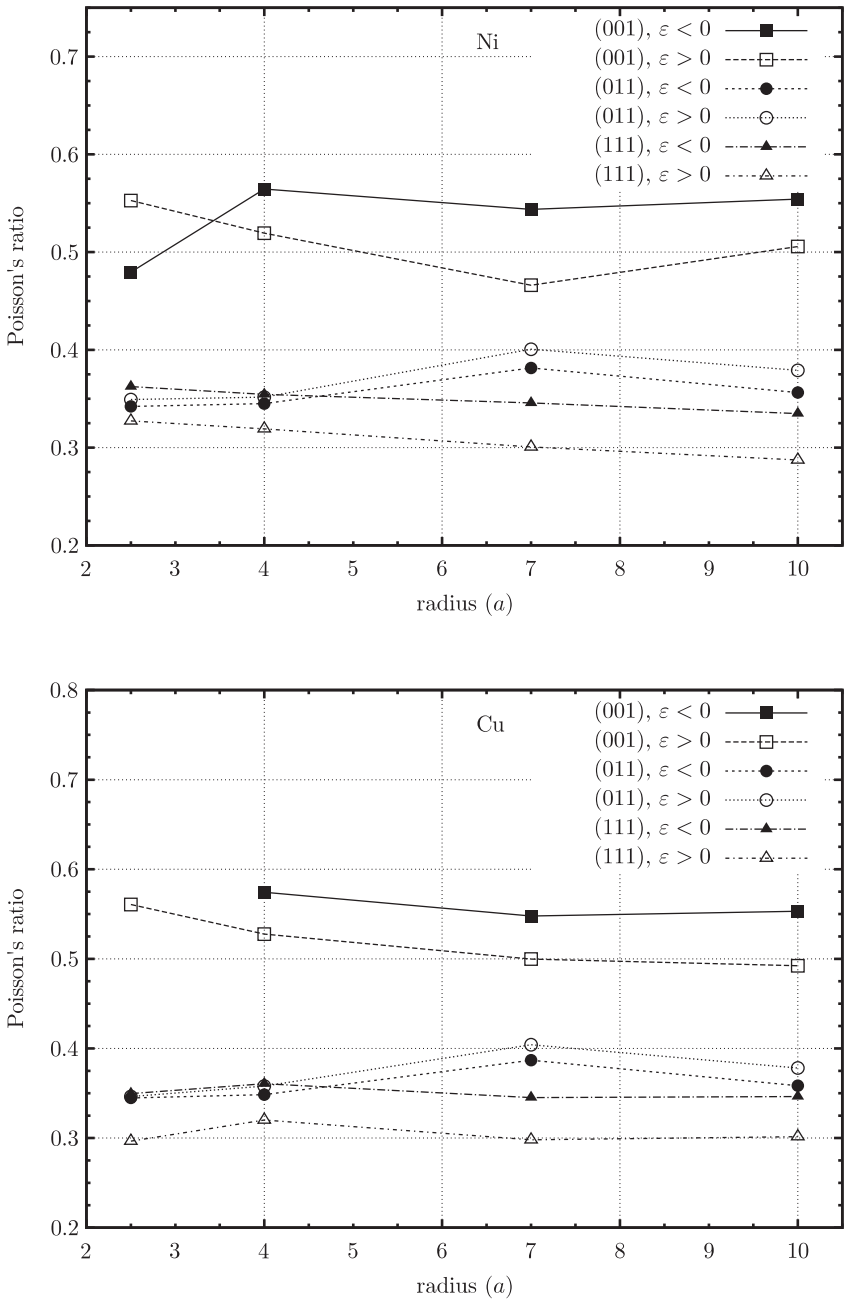

Figure 13. Dependence of Poisson's ratio on the radius and crystallographic orientation of the nanorods

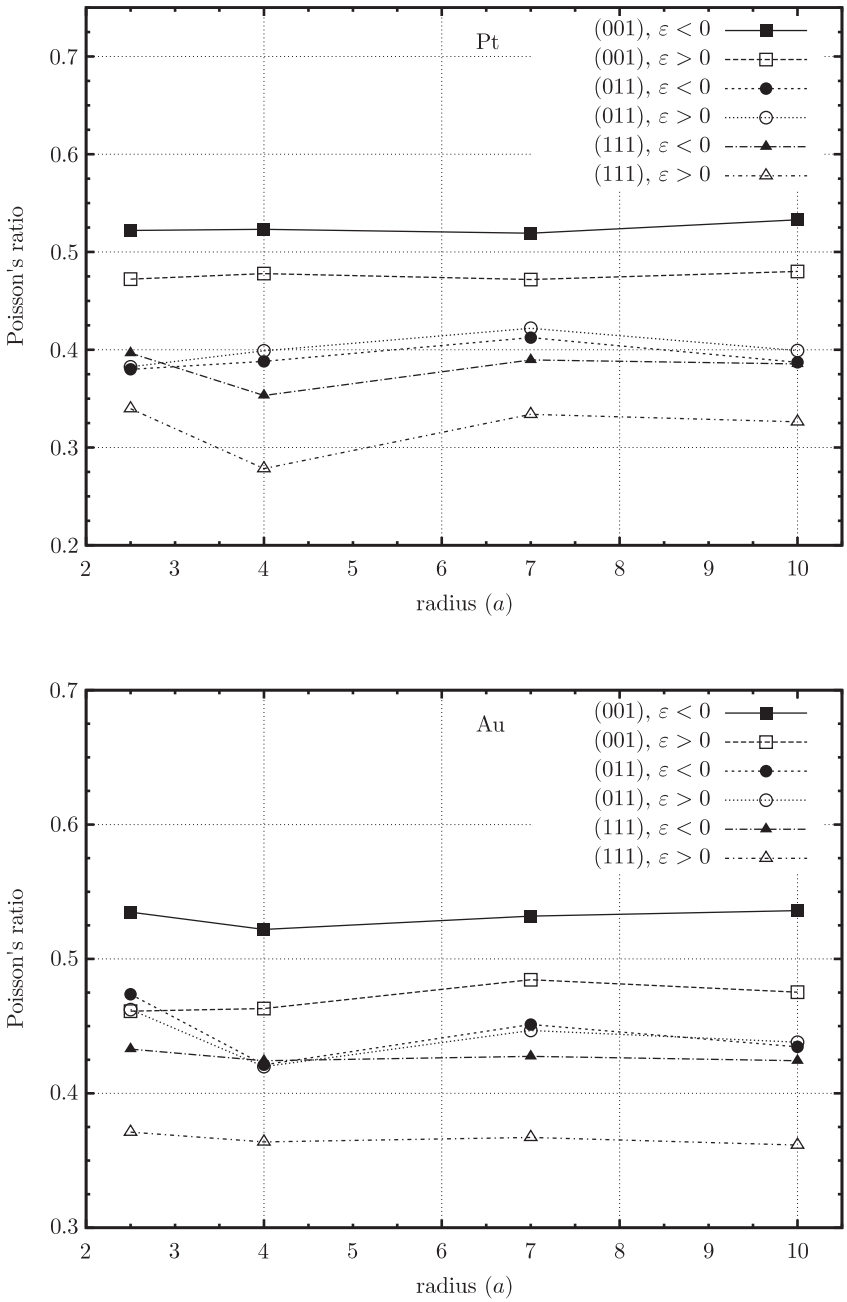

Figure 13 – continued. Dependence of Poisson's ratio on the radius and crystallographic orientation of the nanorods

Table 11 shows the results of a series of tests for different diameters and different crystallographic orientations of a nanorod made of gold. Since the value of the shear modulus does not depend on the nanorod diameter, or its effect is within the margin of error, the modulus for other samples was determined based on simulations performed for one diameter – $14a$. The results for the tested nanorods are presented in Figure 15.

Table 11. Values of the shear modulus G (GPa) for gold nanorods

label	orientation	diameter [a]	frequency [GHz]	modulus G [GPa]
Au-001-2.5	(001)	5	17.8	50.8
Au-001-4	(001)	8	19.3	53.8
Au-001-7	(001)	14	20.0	53.6
Au-001-10	(001)	20	20.2	53.9
Au-011-2.5	(011)	5	12.8	24.9
Au-011-4	(011)	8	14.9	32.4
Au-011-7	(011)	14	14.9	29.7
Au-011-10	(011)	20	15.1	30.3
Au-111-2.5	(111)	5	13.2	27.7
Au-111-4	(111)	8	14.0	28.0
Au-111-7	(111)	14	14.3	27.9
Au-111-10	(111)	20	14.5	28.3

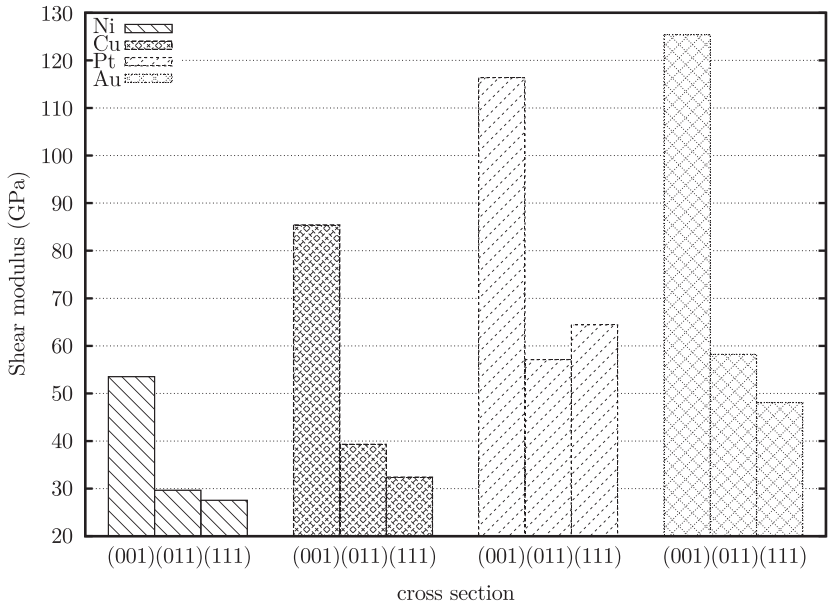

Figure 15. Dependence of the shear modulus on the crystallographic orientation of the cross-section for nanorods $14a$ in diameter

A characteristic feature is the twofold difference between the values for the [001] direction and the corresponding values for the directions [011] and [111], the latter two being similar in magnitude. This indicates a relationship between the shear modulus and the shape of the Wigner-Seitz cell.

Table 12 shows the values of G obtained in the conducted numerical experiments (columns "simulation") and the values obtained from the calculations based on the constants (columns "tables"). The last column gives the shear modulus for a polycrystalline body.

Table 12. Values of the shear modulus G (GPa) for the investigated nanorods

element	(001)		(011)		(111)		polycrystals
	tables	simulation	tables	simulation	tables	simulation	
Ni	124.2	125.4	79.5	58.2	58.9	48.1	76
Cu	75.6	85.4	44.7	39.3	30.1	32.4	48
Pt	76.5	116.4	76.5	57.1	54.8	64.4	61
Au	42.0	53.5	26.2	29.6	18.8	27.5	27

The difference between the values of the shear modulus obtained from the calculations, and the values determined from the elastic constants shown in Table 12 is as big as 30%. It is difficult to determine with certainty whether this is caused by the size of the nanostructures or by the selected calculation method. In qualitative terms the results are in line with the expectations – the maximum value of G was obtained for the (001) cross-section.

The values of the shear modulus calculated from the previously defined Young's modulus and Poisson's ratio for nanorods with the cross-sections (001) and (011) differ by less than 10% from the corresponding values determined from the frequency of torsional vibrations. The ratios calculated by two different and independent methods are comparable, which indicates the internal consistency of the adopted model.

3.4. Propagation velocity of mechanical waves

The obtained propagation velocities of mechanical waves are close to the sound velocities in polycrystalline solids of 4970, 3570, 2680 and 1740 m/s for Ni, Cu, Pt and Au, respectively. A weak dependence of the mechanical impulse velocity on the sample diameter is observed in the obtained results, while there is a clear dependence of velocity on the direction of signal propagation. An increase in the velocity with an increase in diameter is due to the decreasing density and increasing value of Young's modulus. The noticeable convergence of the values obtained for nanorods with the sound velocity in bulk metals shows that the phenomena associated with the transport of mechanical energy proceed similarly at the nanoscale as in continuous media.

3.5. Yield point

The onset of plasticity associated with the occurrence of dislocation and transition of the crystal to a lower energy state is clearly visible as a jump in the sample's energy curves and as a top of knee on the stretch curves (Figure 4). The rapidity of this change is associated with achieving a state in which there is a sudden increase in the number of dislocations and the material becomes permanently deformed.

Plots in Figure 2 show the effect of the crystallographic plane and the direction of the load on the limit strain (yield point) for each of the elements. Plots in Figure 3 show the effect of the crystallographic plane and the direction of the load on the limit stress (yield point). A characteristic feature of all the analysed elements is the stabilization of the limit strain and limit stress values that is observed starting from the rod diameter of approx. $15a$ and the irregularity of this relation for diameters smaller than $8a$.

Plots in Figure 4 show, in the form of a stress-strain curve, the investigated range of strain and the effect of crystallographic planes on the stretching of the sample. A characteristic feature of these curves is the weak effect of the sample radius on the elastic strain. Another feature common for all the obtained results and characteristic for each element is the value of the stress in the region where the sample deforms permanently – the value is independent of both the diameter and the crystallographic direction.

Plots in Figure 4 also show that:

1. samples stretched in the [001] direction maintain a constant value of Young's modulus over the entire elastic range, from zero to the yield point;
2. samples compressed in the [111] direction maintain a constant value of Young's modulus over the entire elastic range, from zero to the yield point;
3. the material becomes more elastic during stretching (Y decreases) with the strain increasing in the [011] direction;
4. the material becomes more rigid during compression (Y increases) with the strain increasing in the [011] direction;
5. Young's modulus of the sample strained in the [011] direction varies over the entire range of elastic strain, compression and stretch;
6. during stretching in the [011] direction, immediately before reaching the yield point ($\varepsilon \approx 0.02 \div 0.05$), the value of Young's modulus is close to zero;
7. during compression in the [011] direction, immediately before reaching the yield point ($\varepsilon \approx 0.02 \div 0.05$), the value of Young's modulus is close to zero;
8. for the same value ε, the resultant stress in the [001] direction is about 1.5 times lower for compression than for stretching, while for the [011] direction the resultant stresses are about 2 times higher for compression than for stretching;
9. the stresses generated during the sample loading in the [111] direction are similar for compression and stretching.

3.6. Stability of nanorods during compression

Let us assume that the formulas valid for massive bodies apply also to nanorods. The critical force at which the compressed rod loses stability (buckling) is determined from Euler's criterion:

$$F = \frac{\pi^2 Y J}{(\kappa L)^2} \tag{26}$$

where $J = \pi D^4/64$ – the moment of inertia of a circular cross section; κ – the coefficient depending on the method of fastening the ends assuming values from 0.5 for rigid fastening of both ends to 2 for a free end. The critical strain can be obtained from:

$$\varepsilon_{cr-} = \left(\frac{\pi D}{4\kappa L}\right)^2 \tag{27}$$

Table 13 contains the values of critical strain for three values of κ: 0.5, 1.0 and 2.0; the nanorod diameter is given in units of crystal lattice constant a; the length was $50a$. Although the values larger than 0.1 have no physical meaning as they exceed the scope of the linear theory of elasticity, they have not been left out from the table.

Table 13. Values of critical strain for the investigated nanorods

$D[a]$	κ		
	0.5	1.0	2.0
3	0.142	0.036	0.009
5	0.395	0.099	0.025
8	1.011	0.253	0.063
14	3.095	0.774	0.193
20	6.317	1.579	0.395

Permanent deformation of the material begins when the strain reaches $\varepsilon \approx 0.05$ and it can be seen that for rigid fastening, where $\kappa = 0.5$, there is no buckling for any of the diameters before the yield point is reached. For $\kappa = 1$ buckling can occur before the yield point is reached for rods $3a$ in diameter. If the loaded end were free, *i.e.* $\kappa = 2$, buckling can occur before the yield point for nanorods with diameters of $3a$, $5a$ and $8a$. The coefficient κ for nanorods is related not only to the method of fixing the ends, but also to the fact that thermal vibrations may initiate a loss of stability by leading to deviations from the equilibrium position. Taking into consideration the uncertainty of whether Euler's formula can be directly applied in the discussed situation and that concerning the value of the coefficient κ to be adopted in the described experiments, a curve representing the maximum deviation from the state of equilibrium as a function of strain has been drawn. A hypothetical curve for platinum for the [001] direction is shown in Figure 16.

The increase in the deflection of the nanorod axis that is apparent in the graph occurs only when the yield point has been reached, therefore, the stability is not lost earlier. The increase in the deflection after reaching the yield point is caused by the onset of slips.

4. Conclusions

The conducted systematic studies of monocrystalline nanorods showed the effect of the direction of the load on the mechanical properties, while the corresponding effect of the nanorod diameter was observed only for rods with

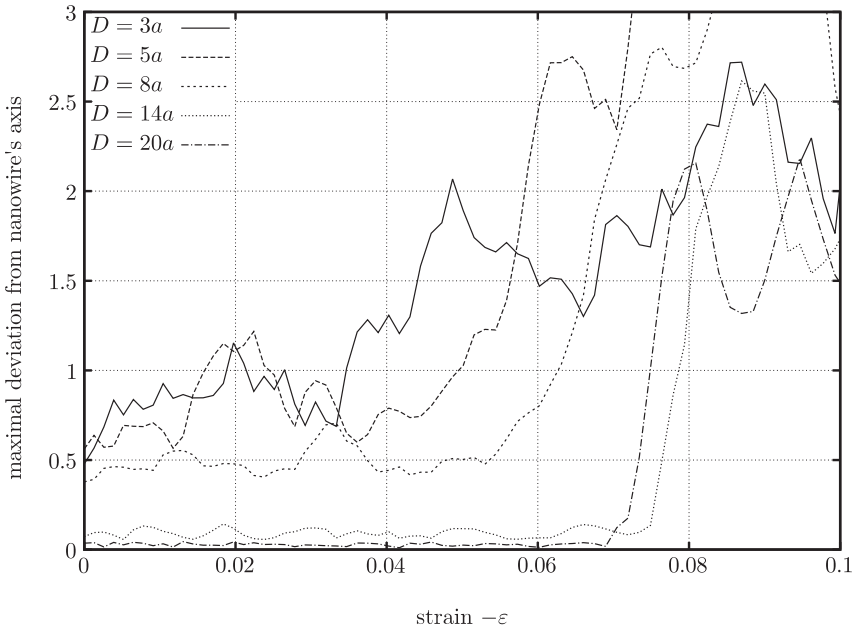

Figure 16. Maximum deviation of the compressed rod axis (platinum, [001] direction)

a diameter below 8 lattice constants. The analysis of the obtained results showed that Young's modulus was highest measured in the [111] direction and remained invariant when the direction of the load was reversed. Its value was lowest when measured in the [001] direction, in this case it was smaller by a factor of 20 for compression compared with stretching. For the [011] direction it was 50 times higher for compression compared with stretching. The values of Poisson's ratio and shear modulus were the highest for the load in the [001] direction, and the lowest for the [111] direction. Beyond the yield point slips were observed in the planes of densest packing (111), regardless of the direction of the load, and they always originated from the outer surface of the nanorod.

The described dependence of the mechanical properties of the nanostructures on the type of load (compression vs. stretching), not considered in the literature, still requires confirmation by comparison with experiment and with more accurate (ab initio) computational approaches.

The obtained results reveal that coming up with a correct nanomechanical model requires the use of different material constants depending on the mechanics of the system which they describe. As in the case of macroscopic systems, material constants offer a correct description only for strains below 2%. For strains in the order of $\pm 80\%$ of the strain required to break the nanostructure, it is sufficient to use a quadratic function to describe the dependence $\sigma(\varepsilon)$. In the entire range of elastic strains, the relation $\sigma(\varepsilon)$ can be described by a cubic polynomial (with an uncertainly below 8%).

The presented analysis showed that the approaches used in the theory of elasticity and strength of materials can be used for nanostructures comprising more than 1000 atoms. However, all the characteristics of the materials should and may be obtained computationally using MD. A description of the behaviour of a nanostructure under load may be obtained by strength of materials methods, while for complicated cases the finite element method can be employed whereby it becomes possible to create models whose sizes exceed those admitted by particle methods.

Acknowledgements

This work was supported by grants N519 024 32/3053 and N519 577 838 of the Polish Ministry of Science and Education.

References

[1] Petrova H, Perez-Juste J, Zhang Z, Zhang J, Kosel T and Hartland G V 2006 *J. Mater. Chem.* **16** 3957
[2] Song J, Wang X, Riedo E and Wang Z L 2005 *Nano Lett.* **5** 1954
[3] Jing G Y, Duan H L, Sun X M, Zhang Z S, Xu J, Li Y D, Wang JX and Yu D P 2006 *Phys. Rev. B* **73** 235409
[4] Marszałek P E, Greenleaf W J, Li H, Oberhauser A F and Fernandez J M 2000 *PNAS* **97** 6282
[5] Elechiguerra J L, Reyes-Gasgab J and Yacaman M J 2006 *J. Mater. Chem.* **16** 3906
[6] Cuenot S, Fretigny C, Demoustier-Champagne S and Nysten B 2004 *Phys. Rev. B* **69** 165410
[7] Ji C, Park H S 2007 *Nanotechnology* **18** 305704
[8] Guo J-G and Zhao Y-P 2007 *Nanotechnology* **18** 74306
[9] Afanasyev K A and Sanso F 2007 *Nano Lett.* **7** 2056
[10] Steinmann P, Elizondo A and Sunyk R 2007 *Modelling Simul. Mater. Sci. Eng.* **15** 271
[11] Hoover W G 1985 *Phys. Rev. A* **31** 1695
[12] Brańka A C and Wojciechowski K W 2000 *Phys. Rev. E* **62** 3281
[13] Sutton A P and Chen J 1990 *Long-range Finnis-Sinclair potentials*, *Philos. Mag. Lett.* **61** 139
[14] Çagin T, Qi T, Li H, Kimura Y, Ikeda H, Johnson W L and Goddard W A III 1999 *Bulk Metallic Glasses, MRS Symposium Series* **554** 43
[15] Ballato A 1996 *IEEE Trans.* **43** 56
[16] Cazzani A and Rovati M 2003 *Int. J. Solids Struct.* **40** 1713
[17] Turley J and Sines G 1970 *J. Phys. D: Appl. Phys.* **4** 264
[18] Wojciechowski K W 2005 *Comp. Meth. Sci. and Tech.* **11** 73
[19] Kleijnen J P C 1995 *Euro. J. Oper. Res.* **82** 145
[20] Diao J, Gall K, Dunn M and Zimmerman J 2006 *Acta Materialia* **54** 643
[21] Hoffmann S, Ostlund F, Michler J, Fan H J and Zacharias M 2007 *Nanotechnology* **18** 205503
[22] Landau L D and Lifshitz E M 1980 *Statistical Physics*, Butterworth-Heinemann
[23] Table by MIT 2007 *ps4 07.pdf*, ocw.mit.edu